© 2017. Published by The Company of Biologists Ltd | Development (2017) 144, 4125-4136 doi:10.1242/dev.154096

RESEARCH ARTICLE

Synaptic input as a directional cue for migrating interneuron precursors

Annika K. Wefers[1,2,*], Christian Haberlandt[2], Nuriye B. Tekin[3], Dmitry A. Fedorov[2], Aline Timmermann[2], Johannes J. L. van der Want[4], Farrukh A. Chaudhry[3], Christian Steinhäuser[2], Karl Schilling[1] and Ronald Jabs[2,‡]

ABSTRACT

During CNS development, interneuron precursors have to migrate extensively before they integrate in specific microcircuits. Known regulators of neuronal motility include classical neurotransmitters, yet the mechanisms that assure interneuron dispersal and interneuron/projection neuron matching during histogenesis remain largely elusive. We combined time-lapse video microscopy and electrophysiological analysis of the nascent cerebellum of transgenic Pax2-EGFP mice to address this issue. We found that cerebellar interneuronal precursors regularly show spontaneous postsynaptic currents, indicative of synaptic innervation, well before settling in the molecular layer. In keeping with the sensitivity of these cells to neurotransmitters, ablation of synaptic communication by blocking vesicular release in acute slices of developing cerebella slows migration. Significantly, abrogation of exocytosis primarily impedes the directional persistence of migratory interneuronal precursors. These results establish an unprecedented function of the early synaptic innervation of migrating neuronal precursors and demonstrate a role for synapses in the regulation of migration and pathfinding.

KEY WORDS: Cerebellum, Interneuron precursor cells, Migration, Pax2, Synapses, Mouse

INTRODUCTION

During development of the vertebrate nervous system, neuronal precursors migrate extensively before they reach their adult positions and terminally differentiate (Valiente and Marín, 2010). Both in the developing forebrain and cerebellum, projection neurons destined to form cortical structures originate in the ventricular epithelium, from where they follow a radial route to reach their adult positions. Precursors of inhibitory interneurons, on the other hand, follow more varied routes to reach their target positions, which generally include extensive tangential relocations (Goldowitz and Hamre, 1998; Letinic et al., 2002; Tan et al., 1998). The eventual establishment of efficiently wired CNS circuits is dependent on a precise coordination of these morphogenetic migrations (Marín et al., 2010). In fact, increasing numbers of neurologic and psychiatric conditions are being associated with neuronal migration deficits (Barkovich et al., 2012; Peñagarikano et al., 2011; Rivière et al., 2012).

In contrast to signals and mechanisms subserving cortical projection neuron migration (Jossin and Cooper, 2011; Rice and Curran, 2001), our mechanistic understanding of interneuronal pathfinding, dispersal and eventual matching with projection neurons is still rather fragmentary (Marín et al., 2010). Cortical inhibitory interneurons are either generated late in ontogenesis or have to migrate for extended periods to their final positions (Leto et al., 2009; Rymar and Sadikot, 2007). Consequently, they have to navigate the nascent lattice formed by earlier settled projection neurons to reach their specific target areas. A key question is whether and how the latter may direct interneuron migration and maturation to assure the generation of properly functioning CNS microcircuits. Intriguingly, an increasing body of evidence indicates that the mobility of neuronal precursors, including immature interneurons, is sensitive to neurotransmitters (Bortone and Polleux, 2009; de Lima et al., 2009; Komuro and Rakic, 1993; Manent and Represa, 2007).

Here, we follow up on this lead and ask how neural communication might affect corticogenesis, and in particular directed interneuron migration in the cerebellar cortex. This cortical structure seems uniquely suited to address such a general question: compared with the forebrain cortex, the cerebellar cortex is evolutionarily rather conserved (Bell et al., 2008). It is constituted by a limited number of genetically well characterized cell types with distinct developmental histories (Goldowitz and Hamre, 1998; Schilling et al., 2008). Its inhibitory interneurons, and particularly those in the molecular layer (ML), arguably form one of the largest and best-characterized groups of inhibitory interneurons in the vertebrate CNS (e.g. Markram et al., 2004; Kepecs and Fishell, 2014; Carter and Regehr, 2002; Jörntell et al., 2010; Kim et al., 2014).

Among the first cerebellar neurons formed are Purkinje cells, inhibitory interneurons of the deep nuclei, and inhibitory interneurons of the future granule cell layer (GL). In the mouse, these go through their last mitosis from around embryonic day (E) 10.5-13.5, E10.5-11.5, and E13.5 to postnatal day (P) 1, respectively (e.g. Sudarov et al., 2011; for a recent review, see Leto et al., 2016), and subsequently migrate radially to form the cerebellar anlage. From about E12.5-16, Math1 (Atoh1)$^{+}$ cells migrate from the rhombic lip (Ben-Arie et al., 1997) underneath the pial surface of the cerebellar anlage to form the external granule cell layer (EGL), where they proliferate extensively up to about P15. Math1^{+} cells give rise to all excitatory cerebellar neurons, including granule cells, unipolar brush cells and excitatory cells in the deep nuclei (Machold and Fishell, 2005). Both afferent climbing fibres (Kita et al., 2015; Wassef et al., 1992) and mossy fibres reach the

[1]Anatomisches Institut, Anatomie & Zellbiologie, Medizinische Fakultät, University of Bonn, 53115 Bonn, Germany. [2]Institut für Zelluläre Neurowissenschaften, Medizinische Fakultät, University of Bonn, 53105 Bonn, Germany. [3]Institute of Basic Medical Sciences, University of Oslo, 0317 Oslo, Norway. [4]Department of Clinical and Molecular Medicine, Norwegian University of Science and Technology (NTNU), 7491 Trondheim, Norway.
*Present address: Department of Neuropathology, Institute of Pathology, Ruprecht-Karls-University Heidelberg, 69120 Heidelberg, Germany.

‡Author for correspondence (ronald.jabs@ukb.uni-bonn.de)

C.H., 0000-0002-1571-9662; J.J.L.v.d.W., 0000-0002-7485-4434; R.J., 0000-0001-6612-7678

Received 2 May 2017; Accepted 11 October 2017

Development (2017) 144, 4125-4136 doi:10.1242/dev.154096

cerebellar anlage before or around birth (Ashwell and Zhang, 1992; Grishkat and Eisenman, 1995; Nunes and Sotelo, 1985).

Lastly, inhibitory interneurons resident in the ML are formed over a rather protracted period, from about E15 to P7 (Leto et al., 2009; Sudarov et al., 2011). They have to traverse the nascent white matter (WM), the emerging internal granule cell layer (IGL), and eventually the Purkinje cell layer (PCL) to reach the ML. There, they initially accumulate at the border of the EGL before they take up their adult positions (Leto et al., 2009; Weisheit et al., 2006; Zhang and Goldman, 1996; Simat et al., 2007; Maricich and Herrup, 1999). According to current thought, it is only then that they become synaptically integrated with granule cell afferents and Purkinje neurons, the sole projection neurons of the cerebellar cortex (Schilling, 2013).

In striking contrast to this detailed descriptive understanding, the mechanisms that direct cerebellar interneuron migration and dispersal remain elusive. To address this issue, we combined two-photon time-lapse imaging and patch-clamp recordings to characterize genetically tagged, migrating precursors of cerebellar inhibitory interneurons. Unexpectedly, we found that these precursors in transit are synaptically innervated. Elimination of synaptic exocytosis reduced the speed and, conspicuously, the directionality of migration. These findings establish a hitherto unknown, early synaptic innervation of developing interneurons. Further, they document that such synapses implement a mechanism that allows these cells to properly navigate the nascent cerebellar cortex.

RESULTS

Basic morphological and electrophysiological characteristics of migrating interneuron precursors

In acute cerebellar slices of 7- to 9-day-old mice expressing EGFP from the locus of the paired-box gene *Pax2* (Pfeffer et al., 2002; Weisheit et al., 2006), precursors of ML inhibitory interneurons can be recognized as strongly EGFP$^+$, slender, fusiform cells. They may be found within the prospective WM, the IGL, and the nascent ML, through which they consecutively migrate to reach their adult position. Their morphology and mobility towards the developing ML (Figs 1 and 2, Movies 1-3) allow them to be readily distinguished from the larger, roundish, and already settled inhibitory interneurons of the IGL (‘Golgi cells’), which also express Pax2 (Maricich and Herrup, 1999). Within the ML, newly arrived Pax2-EGFP cells could be readily distinguished from more mature ML interneurons by their strong EGFP signal, their preferential orientation perpendicular to the PCL, and their mobility. After entering the ML, these cells first translocate towards the border of the ML and the EGL (Simat et al., 2007; Weisheit et al., 2006). Upon their subsequent embedding in the growing ML, they rapidly downregulate Pax2 and Pax2-EGFP (Glassmann et al., 2009; Weisheit et al., 2006), and they can be recognized as dimly stained, immobile cells with their long axis preferentially parallel to the PCL (Fig. 2B).

Strongly Pax2-EGFP$^+$, immature precursors of ML inhibitory interneurons (henceforth referred to as ‘Pax2 cells’) were characterized by a high input resistance (R_{in}>1 GΩ in all but 6/176 cells) and a capacitance of 9.4±0.4 pF (mean±s.e.m.). Their whole-cell current pattern (Fig. 3A) was made up by transient and delayed rectifier K^+ currents and voltage-gated, TTX-sensitive Na^+ currents (Fig. S1). We did not observe spontaneous action potentials in these cells. Upon current injection (Fig. 3B), Pax2 cells in the prospective WM (n=7), the nascent IGL (n=8) and the ML (n=10) generated spikelets, but no full action potentials. Their Na^+ current density was 0.7±0.1 pA/µm^2.

This clearly distinguishes Pax2 cells from Pax2-EGFP$^+$ inhibitory interneurons of the GL, which are characterized by a much larger membrane capacitance (47.8±5.3 pF, n=13). This latter value is in excellent agreement with data reported previously (Dieudonné, 1995; Dieudonné, 1998; Elisabetta Cesana et al., 2006). The electrophysiological properties of Pax2 cells are also clearly distinct from those of mature inhibitory ML interneurons, which show spontaneous action potentials of up to 35 Hz and Na^+ current densities exceeding 30 pA/µm^2 (Ruigrok et al., 2011; Southan and Robertson, 1998).

Application of GABA (100 µM) or the $GABA_A$ receptor agonist muscimol (300 µM) to Pax2 cells held at −70 mV consistently resulted in inward currents [0.03±0.01 pA/µm^2 (n=14) and 0.1±0.01 pA/µm^2 (n=13), respectively] that were blocked by bicuculline (100 µM) by about 85% [to 0.001±0.001 pA/µm^2 (n=4) and 0.02±0.01 pA/µm^2 (n=4) for GABA and muscimol, respectively; Fig. 3C]. The reversal potential at the maximal slope conductance was −0±2 mV (n=12), confirming a Cl^--mediated current (Fig. S2A-A″).

Further, these Pax2 cells in transit also express ionotropic receptors of the AMPA/kainate (KA) type (Fig. 3D, Fig. S2B-B″). We noted that Pax2 cells migrating through the WM display significantly smaller KA (300 µM)-induced receptor currents (0.3±0.06 pA/µm^2, n=14; V_h=−70 mV) than those in the ML (0.95±0.13 pA, n=14; P<0.001 for WM versus ML) indicating developmental changes of receptor density or gating properties (Smith et al., 2000), e.g. due to a switch in flip/flop splicing (Monyer et al., 1991). Cyclothiazide (100 µM), an allosteric modulator of the flip versions of AMPA receptors (Partin et al., 1993), potentiated KA-induced responses in Pax2 cells in the WM (by 86±13% at –70 mV, n=12; P<0.01) but not in the ML (15±6%, n=9; P=0.3). NBQX (20 µM) completely blocked KA-induced currents (n=8). Our data are consistent with the reported relative increase of AMPA-receptor flop variants (Monyer et al., 1991) and/or increased hetero-oligomerization (Liu and Cull-Candy, 2002) with ongoing development.

Migrating precursors receive synaptic input

Unexpectedly, we observed spontaneous postsynaptic currents (sPSCs) in Pax2 cells, suggesting that these immature cells in transit receive synaptic input (Fig. 3E-G). sPSCs could be recorded from 15 out of 17 Pax2 cells in the ML and 5/6 cells transiting the nascent IGL. We could not detect sPSCs in Pax2 cells transiting the prospective WM (n=11).

Next, we wanted to confirm that Pax2 cells receive synaptic input while actually migrating. Over a period of several hours these cells travel substantial distances and may traverse the entire cerebellar cortex (Movie 1). We used high-resolution time-lapse video microscopy and selected cells that had moved at least 3 µm (n=35; median 11.2 µm, range 3-43 µm) for subsequent patch-clamp recording. Wash-out of EGFP during recording confirmed that the visually selected cell was impaled by the patch pipette.

Consistent with the above data for cells selected on the basis of their position and morphology alone, Pax2 cells that had migrated immediately before patch-clamping received synaptic input, depending on their position. Eight out of 13 cells in the IGL, 15/19 in the ML, but 0/3 cells in the prospective WM showed sPSCs. The synaptic origin of this activity in Pax2 cells traversing the IGL and ML was supported by the increased rate of miniature PSCs (mPSCs) following application of the Ca^{2+} ionophore ionomycin (3 µM; Fig. 3L-N). This agent increases the intracellular Ca^{2+} concentration and thus enhances release from the readily releasable

Development (2017) 144, 4125-4136 doi:10.1242/dev.154096

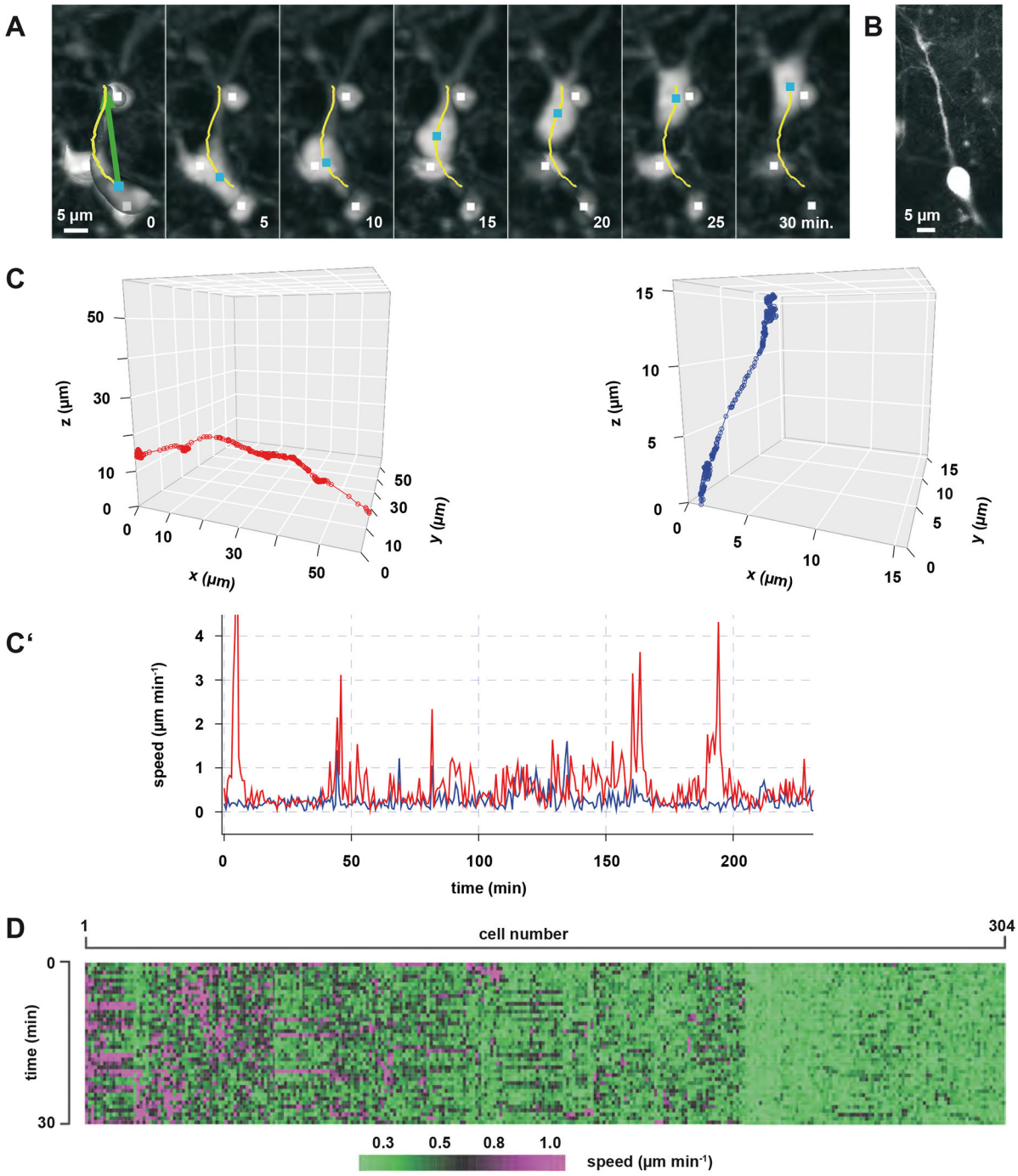

Fig. 1. Morphology and migratory patterns of Pax2 cells. (A) A Pax2 cell (a strongly Pax2-EGFP^{+} immature precursor of ML inhibitory interneurons) (P8) migrating through the IGL. Yellow line is the actual migratory path (length, 22.6 µm) reconstructed from 3D images taken every ~42 s, and based on the cell centre of mass (blue square). Green arrow indicates the displacement of the same cell (18.5 µm). White squares indicate the centres of mass of three Pax2 cells that did not migrate during the observational period. See also Movies 1 and 2. (B) Migrating Pax2 cell. Single confocal plane, optical thickness 4.5 µm. (C) Pseudo-3D plots of a fast (red, left) and a slowly (blue, right) migrating Pax2 cell. Complete 3D stacks were recorded every ~42 s over 4 h. Each point gives the coordinates of the centre of mass over consecutive time points. (C′) Temporal variability of speed for the trajectories shown in C. (D) Summary view of speeds of 304 migrating Pax2 cells, recorded from an acute slice preparation over 30 min in ~42 s intervals. Each colour-coded rectangle represents the speed of individual cells at the indicated time points. Cells with comparable motility are arranged next to each other.

vesicular pool in synaptic terminals. In the WM, in the absence of TTX, no sPSCs were observed in Pax2 cells, even after application of ionomycin.

Analysis of current kinetics distinguished two types of sPSCs with decay time constants of <1 ms and about 12 ms, respectively (Fig. 3E,F,H,I,K upper panel; Fig. 3E,G,K lower panel). Further analysis showed that the former were sensitive to NBQX and APV (i.e. were mediated by ionotropic glutamate receptors; Fig. 3J), whereas the latter were abolished by bicuculline (i.e. mediated by $GABA_A$ receptors; Fig. 3H). As expected for AMPA/KA and $GABA_A$ receptors, the reversal potentials of the fast and slow sPSCs were 0 and –40 mV, respectively (Fig. S3). The rise times of these

Development (2017) 144, 4125-4136 doi:10.1242/dev.154096

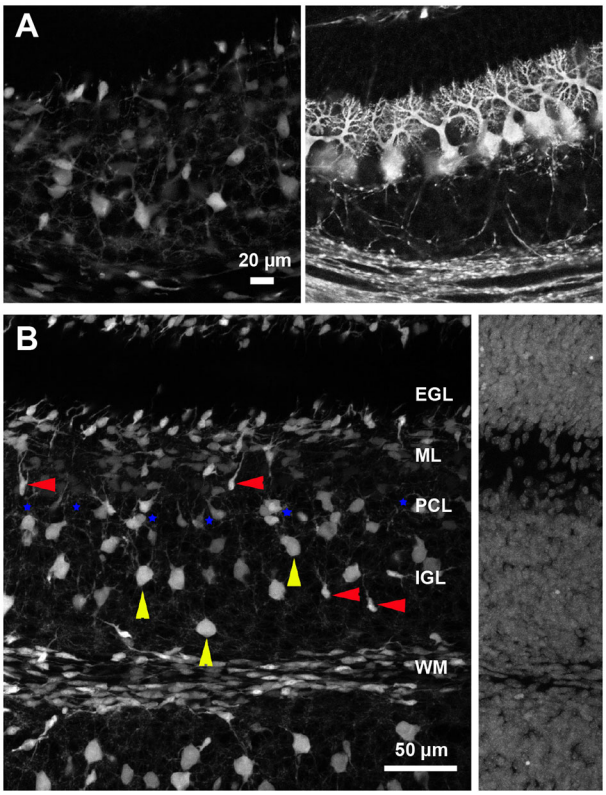

Fig. 2. Morphological characteristics of Pax2 cells. (A) Separate colour channels are shown for the Pax2-EGFP (left) and calbindin 28K (right) signals. The composite of these panels is shown in Fig. 4A. (B) Morphological characteristics used to identify migratory Pax2 cells en route to the molecular layer (ML). These are maximum intensity projections of 60 optical sections through a volume of 375×375×21 µm^3 of the nascent cerebellar cortex (P8, lobule V, position equivalent to the boxed area in Fig. 4A). Exemplary cells identified as (resident) inhibitory interneurons of the granule cell layer are marked by yellow arrowheads. Examples of cells in transit to and through the ML are indicated by red arrowheads. This initial identification based on morphology was corroborated by actual observation of the mobility, or immobility, of these cells as well as by electrophysiology (see main text). The position of the Purkinje cell layer (PCL) is indicated by blue stars (based on nuclear counterstaining). Note that cells in transit to and through the ML show strong EGFP expression. Strongly EGFP$^+$ cells can also be seen at the border between the external granule cell layer (EGL) and the nascent ML, where newly arrived Pax2 cells initially accumulate. By contrast, more mature inhibitory interneurons in the lower parts of the ML show only very weak (pale grey) residual EGFP signal. The EGL may be used as a reference for the EGFP-related background signal. The right-hand panel shows nuclear counterstaining (propidium iodide) to document overall cell density and to facilitate identification of cerebellar cortical layers. The region shown corresponds to the left margin of the left-hand panel. IGL, internal granule cell layer; WM, white matter.

sPSCs were 0.37±0.01 ms for fast-decaying sPSCs (n=1843, 20 cells) and 0.46±0.01 ms for slowly decaying sPSCs (n=384, 17 cells).

All cells with sPSCs (n=43) received glutamatergic input, whereas GABAergic input was less abundant (n=35/43). There was no indication of layer-specific differences in GABAergic or glutamatergic innervation.

On their way into the ML, Pax2 cells migrate sequentially through the WM, the nascent IGL, the PCL, and in the ML up to the EGL (for an overview, see Fig. 4A). To assess the density of presynaptic elements that may contact Pax2 cells en route, we quantified synaptophysin-immunoreactive puncta in these layers. In line with the layer-specific frequency of sPSCs, the density of synaptophysin$^+$, putative presynaptic elements increased from the WM to the ML (Fig. 4B-D). Ultrastructural analysis of Pax2 cells in the lower ML confirmed the occurrence of synaptic structures on these cells (Fig. 5, Fig. S4). This particular location was chosen since expression of Pax2-EGFP allowed the reliable selection of interneuron precursors migrating towards more superficial positions over those that have already settled in the ML (Weisheit et al., 2006). This ultrastructural evidence, together with the fast rise times of the sPSCs, suggests that these sPSCs originate from direct synaptic innervation rather than from transmitter spill-over.

Synaptic innervation and directional persistence of migrating Pax2 cells

To probe the functional significance of this surprising and hitherto unknown synaptic input, we used tetanus toxin (TeNT) and Co^{2+} to abrogate presynaptic vesicular release. Of these agents, TeNT is more efficient as it inhibits exocytosis by cleaving synaptobrevin. We verified the efficacy of these agents in our preparation by monitoring their effect on the frequency and amplitudes of sPSCs recorded from Purkinje neurons. These cells, rather than sparsely innervated Pax2 cells, were chosen because their already strong innervation allows a dependable assessment of synaptic activity. Taking cell-wise sPSC average amplitudes multiplied by the number of events occurring within 5 min as a proxy of synaptic innervation, we observed that TeNT eliminated 99.7±0.2% (mean± s.e.m.) of all synaptic input. Co^{2+} reduced synaptic input by 80.1± 3.7% (five cells, from five slices from two animals, measured before and after Co^{2+} wash-in). Note that remaining sPSCs under Co^{2+} represent essentially spontaneous, action potential-independent release (mPSCs).

We analysed the effects of TeNT on cell motility in three slices obtained from three animals. Migration of 917 Pax2 cells was monitored prior to treatment (exemplary slice shown in Movie 2) and, within the very same volume elements, another 651 cells were monitored following 120 min incubation with TeNT (100 µg/ml). TeNT resulted in robust reductions of Pax2 cell displacement, (average) speed and, intriguingly, the ratio of displacement and total path length, which provides a measure of directionality (Batschelet, 1981; Benhamou, 2004) (Fig. 6; Fig. S5 for methodological details). Sham incubation (without TeNT) did not bring about such changes (Fig. 6, Fig. S5D). Exemplary tracks of control cells and cells after incubation with TeNT are documented in Movie 3.

Mechanistically, the nonspecific antagonist of voltage-gated Ca^{2+} channels, Co^{2+} (used at 2 mM, 20 min wash-in; three slices from three animals), prevents secretion upstream of the site of action of TeNT. It also avoids the protracted incubation needed with TeNT. Furthermore, any potential nonspecific side effects of these two agents may be predicted to be distinct. Intriguingly, the effects of Co^{2+}-reduced synaptic release on cell motility and directionality were virtually identical to those observed following TeNT blockade of exocytosis (Fig. 6).

To probe the loss of directionality following abrogation of presynaptic vesicular release directly and at the high temporal resolution afforded by our sampling rate, we analysed turning angles formed by the track segments ('steps') joining cell positions recorded at subsequent time points, which were separated by ~42 s (see Fig. S6 for a scheme). These angles provide a measure of directional persistence: for cells with high directional persistence, they are centred about zero degrees. By contrast, tracks of cells with low directional persistence are characterized by highly variable

Development (2017) 144, 4125-4136 doi:10.1242/dev.154096

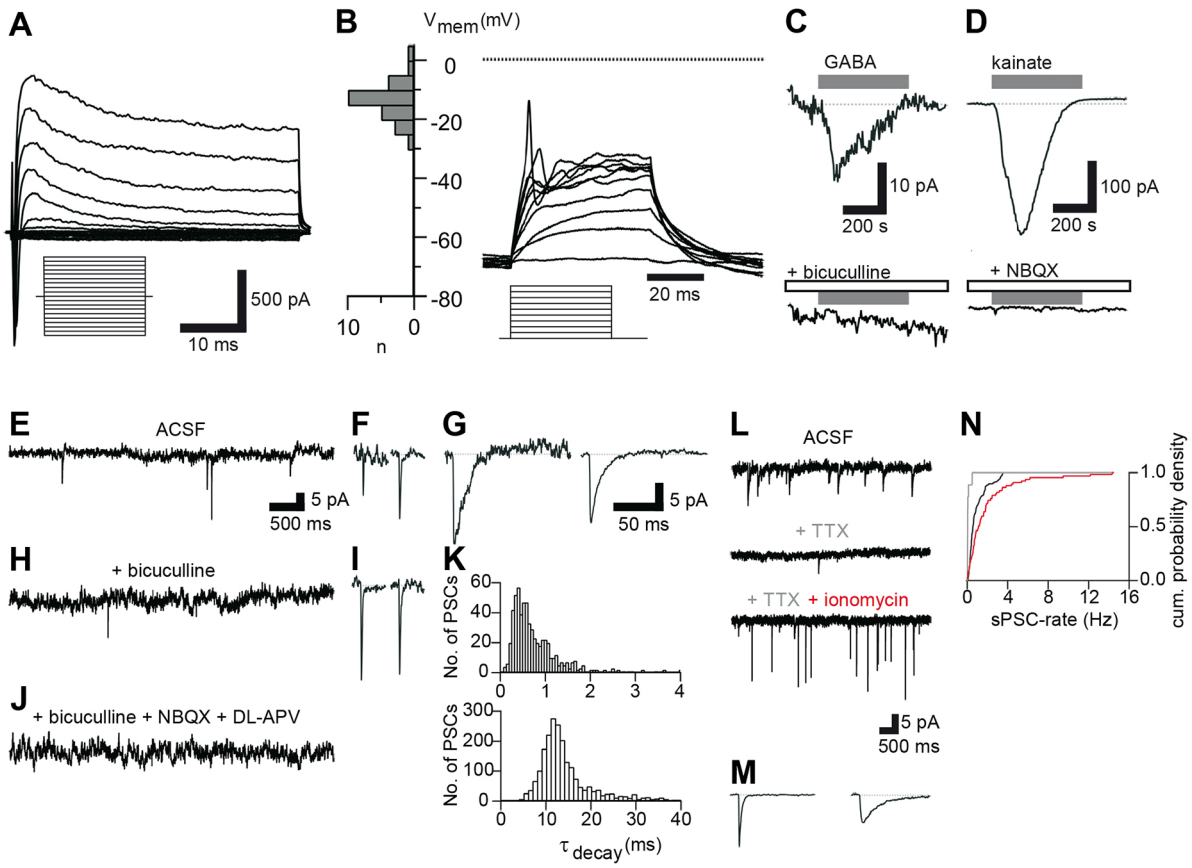

Fig. 3. Pax2 cells receive GABAergic and glutamatergic synaptic input. (A) Whole-cell current pattern of a Pax2 cell (voltage steps from −70 mV to membrane potentials between −160 and +20 mV with 10 mV increment and 50 ms duration, as depicted in the inset), indicating activation of voltage-gated K^+ and Na^+ channels (*n*=176 cells analysed). See also Fig. S1. (B) Pax2 cells fire spikelets upon current injection. Cells prehyperpolarized to −70 mV were injected for 50 ms with up to 72 pA, in 8 pA increments (inset). The histogram on the left gives the frequency of spikelet peak voltages for a total of 25 cells analysed. (C) Inward currents induced by 100 µM GABA (top; holding potential −70 mV; *n*=14 cells analysed plus *n*=13 with application of the $GABA_A$ receptor agonist muscimol) were blocked by 100 µM bicuculline (bottom; *n*=4 cells each analysed with GABA and muscimol). (D) 300 µM KA induced an inward current at −70 mV (top; *n*=14 cells analysed) that could be blocked with 10 µM NBQX (bottom; *n*=8 cells analysed). See also Fig. S2. (E-G) Voltage-clamp recordings from a Pax2 cell in the middle ML held at −80 mV revealed rare sPSCs. Based on their current decay, these could be classified as fast or slow. An individual fast sPSC is shown in F (left; 11 pA, rise 0.3 ms, decay 0.6 ms). The right-hand trace in F shows averaged fast sPSCs (17 pA, rise 0.7 ms, decay 1.5 ms; *n*=4). An individual slow sPSC is shown in G (left; 23 pA, rise 0.7 ms, decay 19.4 ms), and averaged slow sPSCs are depicted on the right-hand side of G (23 pA, rise 0.9 ms, decay 12.1 ms; *n*=20). (H,I) 10 µM bicuculline blocked slowly decaying, but not fast, sPSCs. (I) Left, individual sPSC (26 pA, rise 0.6 ms, decay 0.7 ms); right, averaged sPSCs (23 pA, rise 0.6 ms, decay 1.4 ms; *n*=9). (J) 50 µM DL-APV and 10 µM NBQX inhibited the rapidly decaying sPSCs. (K) Histograms of decay times for fast (top; *n*=490 from 43 cells) and slow (bottom; *n*=1915 from 31 cells) sPSCs. (L-N) Recordings from a cell that had been observed to migrate immediately prior to analysis (*n*=32 cortical and *n*=3 Pax2 cells in WM analysed for postsynaptic currents after proven migration; *n*=3 cells analysed in cortex plus *n*=3 cells in WM with TTX and ionomycin). (L) Voltage-clamp (−80 mV) recordings in ACSF (top trace). Isolated mPSCs in 1 µM TTX (middle trace), the frequency of which was strongly increased by 3 µM ionomycin (lower trace). (M) Averaged fast (left; 13 pA, rise 0.5 ms, decay 2.6 ms; *n*=72) and slow (right; 6 pA, rise 1.6 ms, decay 17 ms; *n*=22) mPSCs recorded in ionomycin. (N) Cumulative probability density of sPSC rates in ACSF (black), in TTX (grey), and with TTX plus ionomycin (red; from traces shown in L). TTX reduced, whereas ionomycin increased, sPSC rates. Scale bars in E apply also to H,J; those in G also to F,I,M. See also Fig. S3.

inter-step angles. Under control conditions (Fig. 7A-C), angles between subsequent steps (Δϕ) were concentrated about 0° in the coronal and sagittal planes, indicating preferentially directional translocation. Following incubation with TeNT (Fig. 7A′,A″) or wash-in of Co^{2+} (Fig. 7C′,C″), the frequency of Δϕ centred about 0° was conspicuously reduced, and larger Δϕ values occurred more frequently (Fig. 7A′,C′). This indicates that, following synaptic silencing, directional persistence of migrating Pax2 cells was reduced. This should not be confused with an overall loss of directed migration. However, the loss of directional persistence makes directed migration much less efficient.

Another way to measure directional persistence is by quantifying the turning angles without reference to anatomical planes (Fig. S6, right). This reduces the dimensionality of the data to one and conveniently allows their statistical analysis with Kuiper's test. This confirmed the visual impression conveyed by the density plots that TeNT (Fig. 7A″) and Co^{2+} (Fig. 7C″) had significant effects on directional persistence (P<0.001), whereas sham incubation (Fig. 7B″) did not (P=0.221).

An intriguing question is whether the effects of synaptic activity on Pax2 cell motility are related to the localized nature of synaptic signalling. Conversely, one might invoke the contribution of synaptic activity to ambient transmitter concentrations to explain the effects observed. To address this question, we blocked ionotropic and metabotropic receptors of glutamate and GABA, but also receptors for purines (P2R) and several cytokines and for neurotrophins [TrkA/B/C (NTRK1-3), p75 (NGFR); see the Materials and Methods for an overview of the receptors targeted

Development (2017) 144, 4125-4136 doi:10.1242/dev.154096

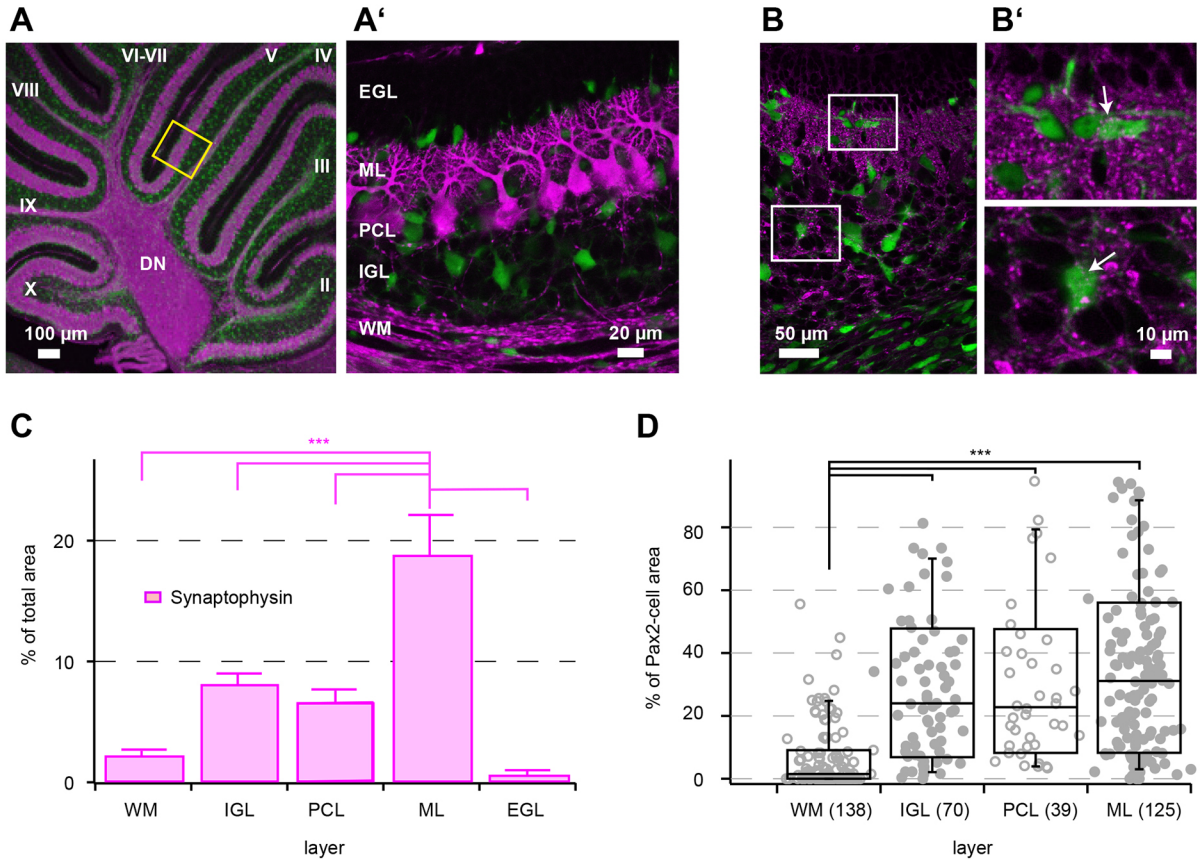

Fig. 4. Distribution and density of Pax2 cells and presynaptic elements in the nascent cerebellar cortex. (A,A′) Parasagittal section through the cerebellar vermis of a P8 animal shows the distribution of EGFP$^+$ Pax2 cells (green) throughout all layers except the EGL. Purkinje cells are stained for calbindin 28K (magenta) and help to delineate the nascent ML and the PCL. Deep nuclei (DN) are also magenta due to the presence of Purkinje cell axon terminals, as is the WM traversed by Purkinje cell axons. The yellow box in A shows the region from where the sections shown in A′ and B were prepared. Roman numerals indicate cerebellar lobules. (A′) Higher magnification focusing on the cerebellar cortex. For separate colour channels, see Fig. 2A. (B) Staining for synaptic vesicles (synaptophysin, magenta). Boxes indicate areas shown at higher magnification in B′. (B′) Synaptophysin$^+$ puncta (examples indicated by arrows) can be found close to Pax2 cells (green) throughout the nascent cerebellar cortex (lobule IX; P8). (C) Layer-specific quantification of synaptophysin$^+$ puncta. Staining density in the nascent ML is consistently higher than in all other layers and the WM. Shapiro-Wilk, $P>0.05$; ANOVA, $P=5.5\times10^{-5}$; ANOVA followed by Tukey, $P<0.001$. Four slices were analysed. (D) Quantification of synaptophysin$^+$ puncta over a mask defined by Pax2 cells shows how potential synaptic contacts close to Pax2 cells increase from the WM to the ML. Numbers of cells analysed are given in parenthesis. Shapiro-Wilk, $P<0.003$; Kruskal–Wallis, $P\approx10^{-30}$; Kruskal–Wallis followed by Dunn-Holland-Wolfe test, $P<0.001$. Four slices were analysed. ***$P<0.001$ in the corresponding post-hoc tests. See Fig. 2 for labels.

by the blockers used], which have previously been shown to impinge on neuronal translocation. In contrast to the elimination of synaptic vesicular release by TeNT or Co^{2+}, global elimination of transmitter action by receptor blockade resulted, at best, in minor and highly variable effects on all motility parameters assessed (Fig. 6).

DISCUSSION

Together, these morphological and functional findings document that precursors of ML interneurons in transit through the cerebellar cortex receive GABAergic and glutamatergic synaptic input, and that synaptic input modulates their migratory behaviour. To the best of our knowledge, synapses have so far not been described on migratory neuronal precursors.

The fast rise times of the postsynaptic currents observed in Pax2 cells are also compatible with ectopic release, i.e. release from presynaptic elements in close contact with cells that lack typical postsynaptic morphology (Matsui and Jahr, 2004). Yet, they rule out spill-over transmission. We prefer the term synaptic, as our ultrastructural data document the existence of morphologically bona fide synapses on Pax2 cells. We note that ectopic release, should it be involved, would still constitute a highly localized signal, functionally equivalent to synapses (as discussed by Matsui and Jahr, 2004).

Although it is well established that neurotransmitters or blockade of their receptors affects neuronal migration (Bolteus and Bordey, 2004; Bortone and Polleux, 2009; Cuzon et al., 2006; de Lima et al., 2009; Komuro and Rakic, 1993; Manent and Represa, 2007; Manent et al., 2005), and notably speed, the present data also unveil a hitherto unknown effect of neurotransmitter signalling on the directionality of migration. This effect was specifically observed following ablation of presynaptic release. Thus, presynaptic elements may function as activity-modulated guideposts for migrating interneuronal precursors that navigate the nascent cerebellar cortex. This conclusion is underscored by the outstanding specificity of tetanus toxin for targeting synaptic release. In particular, this agent does not interfere with neurite outgrowth (Verderio et al., 1999), which might interfere with migration, and which has been observed when (synaptic) release was eliminated by ablation of Munc18-1 (Stxbp1) and Munc13 (Broeke et al., 2010).

At first sight, the distinct effects of ablation of vesicular release and receptor blockade might seem counterintuitive. Yet, if one

Development (2017) 144, 4125-4136 doi:10.1242/dev.154096

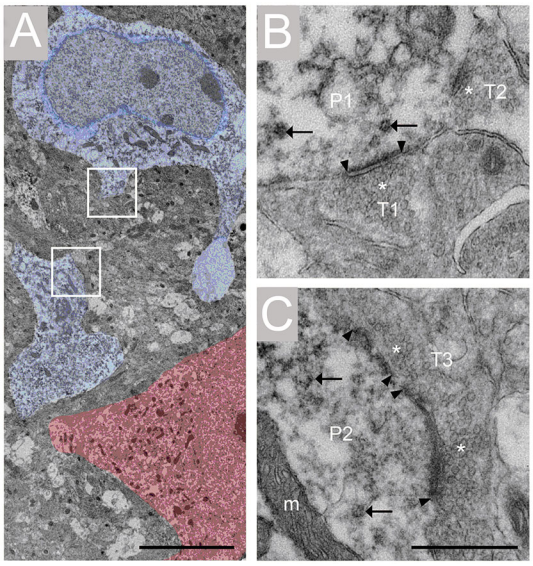

Fig. 5. Ultrastructural details of Pax2$^+$ cerebellar cells. (A) Cells immunopositive for EGFP expressed from the *Pax2* locus (Pax2 cells, blue overlay) are surrounded by neuropil characteristic for the ML. A Purkinje cell perikaryon (pink) is nearby, confirming the position of the Pax2 cells in the lower ML. Pax2 cells display several protrusions, and they are contacted by presynaptic elements. Such synapses are shown at higher magnification in B and C. (B) Higher magnification view of the upper boxed area from A shows two presynaptic elements (T1, T2) contacting the Pax2 cell (P1). (C) Higher magnification view of the lower boxed area from A shows one broad synapse (T3) contacting the Pax2 cell (P2). Note the postsynaptic densities on Pax2 cells (bordered by arrowheads) and clusters of synaptic vesicles in nerve terminals apposing them (asterisks). Arrows indicate peroxidase deposits. Scale bars: 10 µm in A; 0.5 µm in B,C. See also Fig. S4.

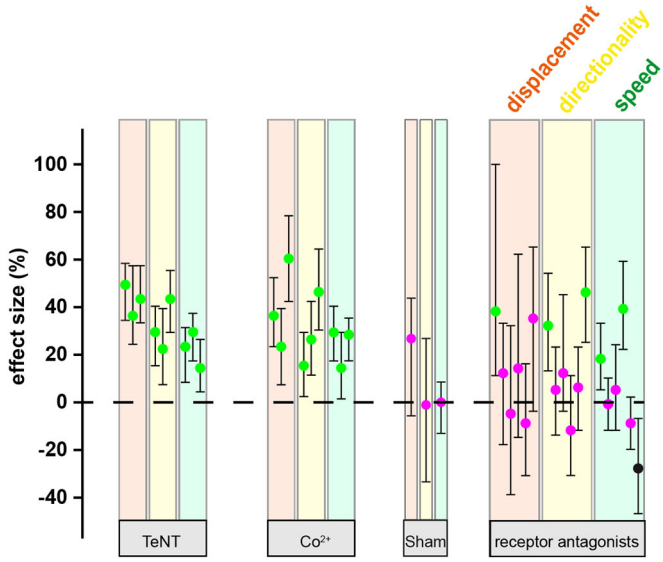

Fig. 6. Synaptic innervation directs the migration of Pax2 cells. Block of presynaptic release with tetanus toxin (TeNT) or Co^{2+} consistently and reproducibly reduced cell displacement, directionality and speed. Shown are medians of effect sizes and their bootstrap-based 95% confidence intervals. For each condition, three slices derived from three animals were analysed, comprising a total of 882 (TeNT) and 1130 (Co^{2+}) cells. The sham slice documented was incubated for 2 h (i.e. as TeNT-incubated slices, but omitting TeNT) in order to identify potential 'run-down' effects due to protracted incubation. No such effects could be detected (total of 262 cells). By contrast, bath application of a cocktail of receptor antagonists blocking ionotropic and metabotropic receptors for glutamate and GABA, purines (P2X and P2Y receptors) and also neurotrophin receptors affected migration only moderately and showed high intra- and inter-experimental variability. Data were obtained from six slices of six animals encompassing a total of 2069 cells. Note that the effects are significant if their confidence interval does not include zero (dashed line). The colour code indicates whether treatment significantly reduced (green dots), increased (black dots), or did not change (magenta dots) the parameter analysed. See Fig. S5 for additional data and methodological details.

contrasts how TeNT (or Co^{2+}) and receptor blockade act on transmitter-mediated signals perceived by migrating cells (Fig. 8), these differences provide a first clue as to how the hitherto unknown synaptic input to migrating neurons may mechanistically control their directionality and locomotion.

Traditionally, effects of transmitters on the motility of neuronal precursors have been surmised to be exclusively due to ambient, paracrine-acting transmitters (Bolteus and Bordey, 2004; Bortone and Polleux, 2009; Cuzon et al., 2006; de Lima et al., 2009; Komuro and Rakic, 1993; Manent and Represa, 2007; Manent et al., 2005), i.e. a non-localized, or isotropic, signal. By contrast, synaptic input, as identified here, results in highly anisotropic signals. Notably, synaptic input onto Pax2 cells does not generate action potentials and thus results in a localized, rather than a propagating, signal. This conclusion may be reached considering that no action potentials, not even spikelets, could be elicited from Pax2 cells by current injections up to 40 pA (see first five sweeps in Fig. 3B, counting from bottom to top), i.e. well beyond the amplitudes of sPSCs recorded from these cells.

Suppression of synaptic release abrogates this anisotropic input to migrating cells. It will eventually also dampen global, isotropic (paracrine) input due to its effect on ambient transmitter concentrations. Yet, as the latter are likely to be regulated in the developing brain primarily by non-synaptic mechanisms (Luhmann et al., 2015; Manent et al., 2005), such as transmitter-permeant anion channels (e.g. Liu et al., 2009), neurotransmitter transporters (possibly working in reverse; see Raiteri and Raiteri, 2015), or insufficient transmitter uptake (by glial cells; e.g. Komuro and Rakic, 1993), synaptic silencing will not effectively shut down isotropic transmitter effects (Fig. 8, middle). By contrast, receptor antagonists eliminate signalling completely and irrespective of its source (Fig. 8, right).

Thus, the distinct effects of blockade of vesicular release and receptors may be rationalized by a model that combines a permissive global (isotropic, paracrine) input with a local (anisotropic, synaptic) instructive signal to regulate neuronal migration and pathfinding. The permissive signal is required to keep the locomotor apparatus of the cell malleable and able to react to a localized (guiding) signal. In the specific absence of localized signals (i.e. following incubation with TeNT or Co^{2+}), cell movements become erratic and disoriented. In the absence of all external signals (i.e. following receptor blockade), cell locomotion initially persists due to the internal inertia of its locomotor system; eventually, though, its motility will also deteriorate, as the decay of its locomotor system is no longer balanced by reorganization dependent on external input.

This model is parsimonious and explains all of the observed effects without the need to invoke some enigmatic, synaptically released agent directing Pax2 cell migration. It provides a consistent and parsimonious explanation for both the relatively high variability of the effects seen following receptor blockade, and the observation that receptor blockade does eventually change cell mobility, when observed over more protracted time periods (but also at much sparser sampling rates) as we did here (e.g. Bolteus and Bordey, 2004; Bortone and Polleux, 2009; Cameron et al., 2009; Cuzon et al., 2006; de Lima et al., 2009; Komuro and Rakic, 1993; Manent

Development (2017) 144, 4125-4136 doi:10.1242/dev.154096

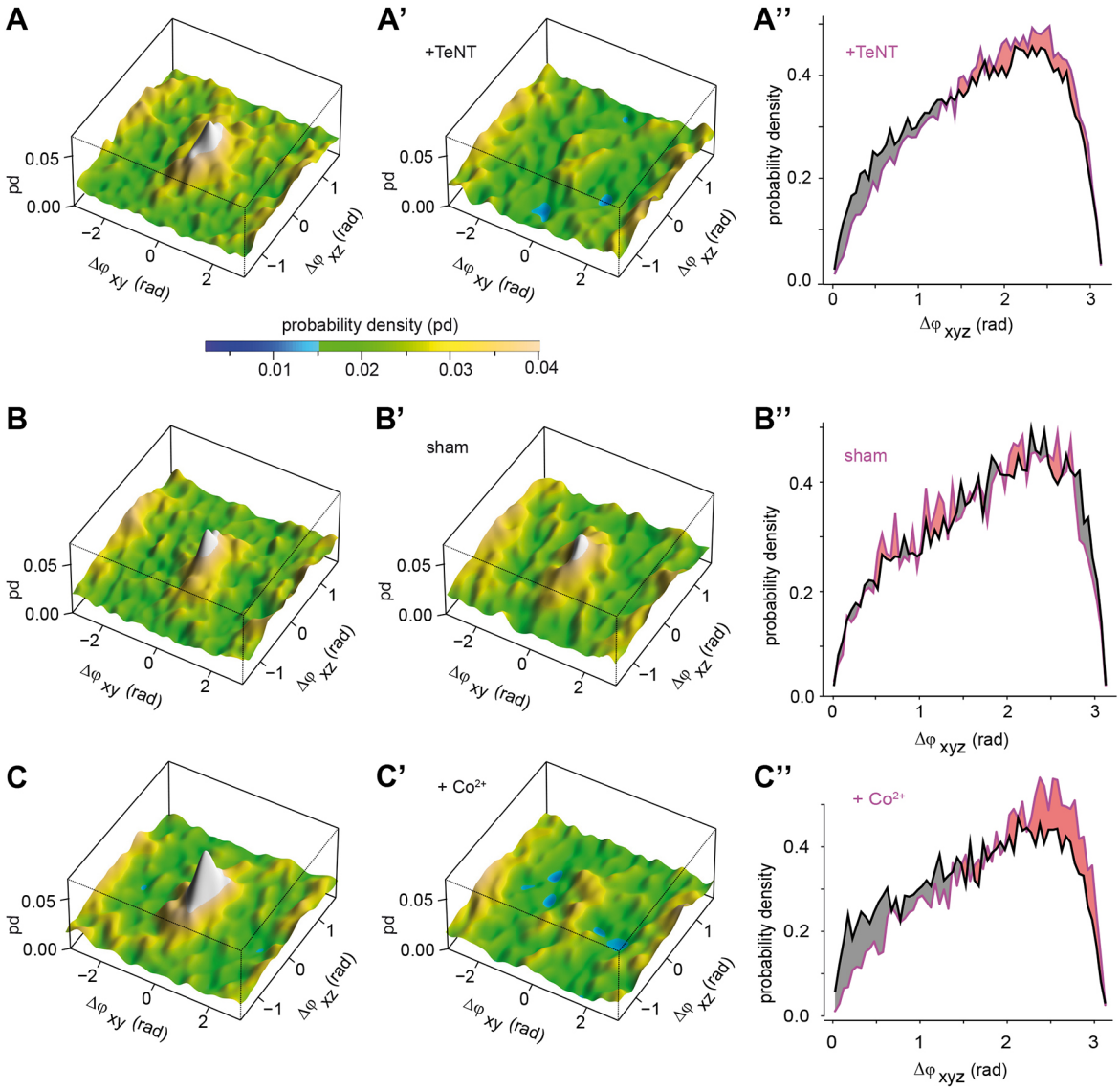

Fig. 7. Synaptic innervation enhances directional persistence of migrating Pax2 cells. Typical probability density maps of between-step turning angles ($\Delta\phi$) of Pax2 cells migrating in acute slices of P8 cerebella. $\Delta\phi$ values were determined as projections in the sagittal ($\Delta\phi_{x,y}$) and coronal ($\Delta\phi_{x,z}$) planes (see Fig. S6 for details). The probability density (colour code) of individual $\Delta\phi$ values is displayed along the *z*-axis. Under control conditions, many $\Delta\phi$ values were close to 0 resulting in a central peak. (A,C) Incubation with tetanus toxin (A, 100 µg/ml) or wash-in of 2 mM Co^{2+} (C) abolished the central peak (A′,C′). This indicates decreased directional persistence. (A″,C″) $\Delta\phi_{xyz}$ angles, determined in 3D before (black traces) and after (magenta traces) incubation with TeNT (A″) or Co^{2+} (C″). Blockade of synaptic release results in a clear-cut shift of turning angles towards higher values (Kuiper's test, $P<0.001$). (B) Sham incubation without TeNT had no substantive effect on the central peak (B′) or on the distribution of $\Delta\phi_{xyz}$ angles (B″) (Kuiper's test, $P=0.221$). Between 7510 and 12740 $\Delta\phi$ values were analysed per condition.

and Represa, 2007; Manent et al., 2005). Further, the model is conceptually equivalent to the well-established context-dependence of axon guidance signalling, where the attractive or repulsive interpretation of one signal may be switched by a second, permissive signal (or internal state) of the receptive cell (see Naoki et al., 2016 and references therein). Third, this model may also be seen as an instance of a more general model in which contrasting local and global effects are integrated to allow cells to steer in shallow gradients and to avoid adaption (Hecht et al., 2011; Xiong et al., 2010). These conceptual parallels might also help to conceive future research to further identify the molecular mechanisms underpinning the observed migratory behaviour.

To date, the mechanisms that direct the fate, differentiation and spatial dispersal of cerebellar inhibitory interneurons remain elusive. Recent experimental evidence (Leto et al., 2009) revealed that postmitotic precursors of these cells retain a considerable degree of plasticity while in transit from the ventricular zone to their adult positions, and are sensitive to, and dependent on, instructive signals received en route. The present results document that migration of inhibitory interneuron precursors is sensitive to presynaptic vesicular release; more significantly, we show that early synaptic activity provides a directional cue for these cells.

This suggests a novel function for released neurotransmitters beyond those established for neural precursor proliferation (e.g. Liu et al., 2005; LoTurco et al., 1995), motility (e.g. Bouzigues et al., 2007; Manent et al., 2005) and network integration (e.g. Ge et al., 2006; for a review see Spitzer, 2006). We demonstrate that transmitters act on developing cells in transit in a highly localized

Development (2017) 144, 4125-4136 doi:10.1242/dev.154096

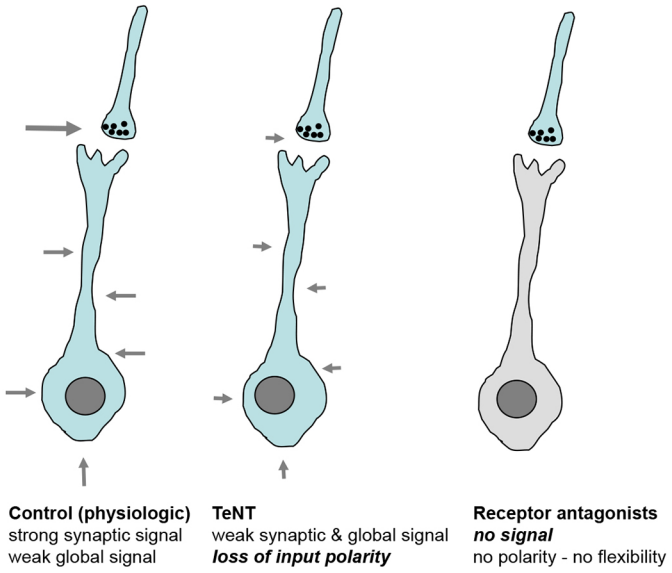

Fig. 8. Model of how neurotransmitters might impinge on the mobility of neuronal precursors. Transmitter action-effect size is symbolized by arrow size. Under physiological conditions, and also with TeNT, isotropic paracrine input keeps the cell in a 'receptive' state, i.e. its internal machinery is plastic and responsive to directive signals (which may come from synaptic input). By contrast, in the absence of all input this plasticity is lost, and the cell initially persists in the state it had immediately before receptor blockade. Eventually, this internal state decays, and cell movement becomes erratic.

manner, indicating a role for synaptic innervation in early neural histogenesis.

Abrogation of synaptic release onto Pax2 cells reduced their displacement by some 40% (Fig. 6). This should give an idea of the size of the effect that synaptic activity may have on the migration and dispersal of basket/stellate cells *in vivo*. Further, the spatiotemporal resolution of the present data allowed us to identify changes in cellular directionality, rather than speed, as the major determinant of displacement. As alluded to above, the robust effect of synaptic input on directionality in terms of directional persistence as described here for Pax2 cells is in keeping with models (Hecht et al., 2011; Xiong et al., 2010) that explain how localized input enables cells to navigate molecular gradients generated by paracrine release and to avoid adaptation.

The migrating Pax2 cells that we analysed (in the P7-9 cerebellar anlage) will eventually settle in the upper part of the ML (Leto et al., 2009, 2011), to which their dendrites will also remain confined (e.g. Rakic, 1972; Sultan and Bower, 1998). There, they will form excitatory synapses with granule cell-derived parallel fibres and inhibitory synapses with each other (for a review and details on the synaptic wiring of ML interneurons, see Schilling, 2013).

Potential candidates providing afferent input to Pax2 cells en route include inhibitory interneurons of the GL and parallel fibres in the lower ML. The latter will not synapse on Pax2 cells analysed here once they have reached the upper ML. However, we consider parallel fibres an unlikely source of developmental synaptic input to migrating Pax2 cells, given that there is no experimental evidence supporting spontaneous or triggered granule cell activity during the critical developmental period analysed here (for a review, see Sassoe-Pognetto and Patrizi, 2013).

GABAergic Purkinje cells, glutamatergic mossy and/or climbing fibres or developmental, intermediate forms of the latter two (Mason and Gregory, 1984) seem more likely candidates to provide (transient) afferents to mobile Pax2 cells. First, they are known to be active during the early postnatal period of cerebellar development (e.g. Puro and Woodward, 1977; Shimono et al., 1976; Sokoloff et al., 2015). Second, at least mossy fibres and climbing fibres are notorious for establishing developmentally transient synapses (e.g. Kalinovsky et al., 2011; Mason and Gregory, 1984; Watanabe and Kano, 2011).

The finding that $Pax2^+$ precursors of (upper) ML interneurons are synaptically innervated in areas not targeted by the afferents of their adult forms implies that they experience a switch in synaptic input as they migrate to their final destinations. This switch would differ qualitatively from the well-known developmental synaptic remodelling that occurs on more mature postmigratory cells to assure adequate matching of pre- and post-synapses (Gianola et al., 2003; Kalinovsky et al., 2011; Watanabe and Kano, 2011; Watt et al., 2009).

As the reduced preparation used here preserves only intracerebellar sources of mossy fibres, i.e. those originating in deep nuclei (Batini et al., 1992), the impact of the mossy fibre system on Pax2 cell migration has probably been underestimated.

Our results identify a novel mechanism that allows synaptic activity in long-distance projections to fine-tune local circuit formation by impinging on interneuron positioning during development.

MATERIALS AND METHODS

Animals

Mice expressing EGFP from the *Pax2* locus (Pax2-EGFP; line BAC#30; Pfeffer et al., 2002; Weisheit et al., 2006) were kept as heterozygotes on a C57BL/6 background. All animal handling was performed in accordance with local governmental and institutional animal care regulations.

Preparation of cerebellar slices

Mice of either sex (P7-9) were anaesthetised and decapitated. Parasagittal slices (200 or 300 µm) were cut from the cerebellar vermis using a vibratome (VT 1000 S or 1200 S, Leica) and collected in ice-cold buffer comprising 87 mM NaCl, 2.5 mM KCl, 1.25 mM NaH_2PO_4, 7 mM $MgCl_2$, 0.5 mM $CaCl_2$, 25 mM $NaHCO_3$, 25 mM glucose, 75 mM sucrose (347 mOsm) gassed with carbogen. The sections were stored for 30 min at 32°C, cooled to room temperature (RT; ~24°C) over a period of 30 min, and transferred to artificial cerebrospinal fluid (ACSF, RT) containing 126 mM NaCl, 3 mM KCl, 1.25 mM NaH_2PO_4, 2 mM $MgSO_4$, 2 mM $CaCl_2$, 26 mM $NaHCO_3$, mM 10 glucose.

Patch-clamp recordings

Slices were viewed with infrared DIC optics. Pax2 cells in lobule IV were identified by their expression of EGFP (using epifluorescence, with a Zeiss Axioskop FS2 or Leica DM 6000 CES microscope) and their distinct morphology. Whereas stationary interneurons of the GL, which also express Pax2, are rounded with a diameter of about 12-15 µm, Pax2 cells are slender with a perikaryon measuring about 12×5 µm. They were typically oriented perpendicular to the PCL while in transit through the cerebellar cortex. Lastly, we note that mature interneurons of the GL, including Golgi cells, showed a characteristic electrophysiological signature and were able to generate action potentials, which unequivocally distinguished them from Pax2 cells. Cells were recorded in the whole-cell mode. During recording, slices were continuously perfused with ACSF, unless stated otherwise. Patch pipettes (borosilicate capillaries) had resistances of 3-4.5 MΩ and were filled with 130 mM KCl, 3 mM Na_2-ATP, 2 mM $MgCl_2$, 0.5 mM $CaCl_2$, 5 mM BAPTA, 10 mM HEPES; or with 130 mM CsCl, 3 mM Na_2-ATP, 2 mM $MgCl_2$, 0.5 mM $CaCl_2$, 5 mM BAPTA, 10 mM HEPES; or with 125 mM K-gluconate, 2 mM Na_2-ATP, 2 mM $MgCl_2$, 0.5 mM EGTA, 10 mM HEPES, 20 mM KCl, 3 mM NaCl; or with 125 mM Cs-gluconate, 2 mM Na_2-ATP, 2 mM $MgCl_2$, 0.5 mM EGTA, 10 mM HEPES, 20 mM CsCl, 3 mM NaCl (all solutions were pH 7.25-7.3; liquid junction potentials corrected for gluconate solutions). EGFP washout was used to confirm that

Development (2017) 144, 4125-4136 doi:10.1242/dev.154096

recordings were actually obtained from Pax2 cells. To allow visualization of cells after EGFP washout, internal solutions also contained 0.05% dextran-conjugated TRITC or 0.1% dextran-conjugated Texas Red (both MW 3000, Molecular Probes). Data were recorded with EPC 8, 9 or 800 amplifiers, filtered at 1-3 kHz, sampled at 0.1-30 kHz, and digitized with DAAD converters (ITC 16 or LIH 1600) controlled by TIDA software (HEKA Elektronik). Test pulses were elicited between −160 and +70 mV (before and after adding TTX, 1 µM), subsequent to applying conditioning pre-pulses (to −110 and −10 mV) to remove current inactivation. AMPA/KA receptors were analysed in solutions containing bicuculline (10 µM) or picrotoxin (50 µM); $GABA_A$ receptors were analysed in solutions containing NBQX (10-20 µM) or CNQX (10 µM); both solutions also contained 10 mM $BaCl_2$, 4 mM 4-AP, 30 µM $CdCl_2$, 1 µM TTX, 50 µM DL-APV or 20-25 µM D-APV, 135 mM NaCl, 5 mM KCl, 2 mM $MgCl_2$, 2 mM $CaCl_2$, 10 mM glucose, 10 mM HEPES (Fig. 3C,D, Fig. S2). Agonists were bath applied. Data were analysed with Igor Pro 6 (WaveMetrics) and MiniAnalysis 6 (Synaptosoft) or PClamp 10 (Molecular Devices). PSCs with amplitudes less than twice the noise level were excluded. All electrophysiological recordings were obtained at RT. Slices for these analyses were obtained from a total of ∼100 animals, and all measurements reported are based on values obtained from at least three slices obtained from animals taken from distinct litters. More typically, data were obtained from 8-12 slices from 5-7 animals from distinct litters. All data recorded were used for analysis.

Imaging

Migration of Pax2 cells was observed in lobules IV and V of a total of 14 acute slices (300 µm) prepared from 14 animals from distinct litters. Slices were kept in modified, 35°C ACSF containing 132 mM NaCl, 3 mM KCl, 1.25 mM NaH_2PO_4, 2 mM $MgCl_2$, 2 mM $CaCl_2$, 20 mM $NaHCO_3$, 10 mM glucose. We blocked presynaptic release by adding either TeNT (100 µg/ml; three slices) or Co^{2+} (2 mM; three slices) to ACSF. One slice was used for sham incubation, and one for long-term observations (up to 4 h) to check for run-down of our preparation. To block postsynaptic receptors, we combined antagonists against ionotropic glutamate receptors of the AMPA/KA (NBQX, 20 µM) and NMDA (D-APV, 25 µM) subtypes, metabotropic glutamate receptors (group I-III: LY341495, 5 µM; mGluR5: MPEP, 10 µM; mGluR1: 3-MATIDA, 40 µM), ionotropic $GABA_A$ receptors (gabazine, 20 µM), metabotropic $GABA_B$ receptors (CGP55845, 4 µM), ionotropic purinergic receptors ($P2X_{1\text{-}6}$: PPADS, 200 µM), metabotropic purinergic receptors ($P2Y_{1\text{-}12}$: suramin, 100 µM; $P2Y_{1,2,4,6,11,12}$: MRS2279, 0.5 µM), cytokine receptors including TrkA/B/C, p75 and others (NGF inhibitor: Ro 08-2750, 5 µM; pan-Trk inhibitor: GNF5837, 0.5 µM; JAK2, FLT3 and TrkA inhibitor: lestaurtinib, 0.5 µM). For these pharmacological studies, we analysed cells from a total of six slices from six animals from distinct litters.

Time-lapse recordings were performed either in *x*,*y*,*t* (3D) with a Zeiss confocal LSM5 Pascal [argon laser (Lasos), excitation at 488 nm], or in *x*, *y*,*z*,*t* (4D) with a Leica LSM TCS-SP5 and two-photon excitation [pulsed IR laser (Mai Tai BB, Newport/Spectra Physics), excitation at 980 nm]. For 3D time-lapse recording, images (217×217 μm^2) were taken every 10 s for up to 4.5 h from an individual Pax2 cell, which was manually kept in the focal plane. In 4D time-lapse recording, volumes of 456×456×30 μm^3 were imaged every 42 s up to 4 h. If the *z*-drift was >4 µm, *z*-settings were readjusted. Offline *xyz*-drift correction was based on the stationary Golgi cells. For quantitative analysis of Pax2 cell migration, centres of mass calculated from isosurfaces were tracked over time (Imaris 7.5.1, Bitplane). Only cells that were visible during at least 80% of the observation time were included. Speed was calculated from the distance the cells travelled between two successive observation points. Displacement represents the straight line distance between the start and end points of a cell trajectory, and directionality is the ratio of displacement and length of the entire trajectory.

Angles between subsequent migratory steps were measured in the sagittal plane (i.e. the plane of slice sectioning) and in the coronal plane. For calculation of probability density plots, we accounted for the fact that angular changes measured in the sagittal plane are continuous at ±π radians, and those in the coronal plane at ±0.5 π radians. Data-based smoothing kernels were determined as described by Jones et al. (1996) and Sheather and Jones (1991).

Electron microscopy

Transgenic mice expressing EGFP under the control of the *Pax2* promoter were anesthetized and perfusion fixed transcardially with 0.01 M PBS (pH 7.4) containing 4% paraformaldehyde (PFA) and 0.05% glutaraldehyde at P8. Cerebella were sectioned using a vibratome (50 µm). Pre-embedding immune-peroxidase staining and electron microscopy were performed as previously described (Boulland et al., 2003). Briefly, sections were treated with 1 M ethanolamine-HCl (pH 7.4) and 1% H_2O_2, followed by incubation overnight with rabbit anti-GFP antibodies (1:1000; Rockland Immunochemicals, 600-401-215) in 10% newborn calf serum in 0.1 M Tris/HCl (pH 7.4) containing 0.3 M NaCl. The sections were then incubated with biotinylated anti-rabbit antibodies, streptavidin-peroxidase complexes, and finally with diaminobenzidine and 0.1% H_2O_2. Samples of stained tissue were dissected out, treated with 1% OsO_4 in phosphate buffer, dehydrated in a graded ethanol series and propylene oxide and embedded in Durcupan ACM (Sigma). Subsequently, ultrathin sections were cut and lightly contrasted with 2% uranyl acetate and 0.3% lead citrate. The samples were examined with a Tecnai CM10 electron microscope (FEI).

Alternatively, the DAB reaction product from immune labelling for GFP was intensified with a modified gold-substituted silver peroxidase technique (van den Pol and Gorcs, 1986). After washing DAB-reacted slices with 0.1 M Na cacodylate buffer (CB; pH 7.6), they were fixed in 0.2% glutaraldehyde in CB, and then osmicated in CB with 1% OsO_4 and 1.5% potassium hexacyanoferrate for 15 min. After dehydration in a graded ethanol series, they were flat-embedded in Epon. Semi-thin sections (1 µm) were cut on an LKB Ultratome, stained with Toluidine Blue and used for orientation. Ultrathin sections (50-100 nm) were collected on Formvar-coated grids, counterstained with uranyl acetate and lead citrate, and examined with a Philips CM 100 transmission electron microscope (FEI).

Immunohistochemistry

PFA-fixed slices (50 µm) were blocked with 2% normal goat serum in PBS for 2 h and incubated at 4°C with antibody G95 against synaptophysin (1:500) (Ikin et al., 1996) or against calbindin D28K (1:4000; Swant, #300) overnight. Alexa-546 goat anti-rabbit or goat anti-mouse secondary antibodies (1:500; Molecular Probes) were applied for 2 h. Confocal images were acquired using a Leica TCS SP2 system (excitation, 488 nm/543 nm; *z*-width, 115 nm). To obtain a measure of the density of presynaptic elements in cerebellar layers, we measured the fraction of pixels indicating synaptophysin immunoreactivity separately for each layer. To assess whether Pax2 cells might be contacted by synaptophysin$^+$ terminals, we first generated a mask based on the EGFP signal to delineate Pax2 cells. Next, colocalization of EGFP and synaptophysin immunoreactivity was quantified as described by Costes et al. (2004). Computation was performed with Imaris.

Reagents

NBQX, D-APV, LY341495, lestaurtinib, GNF5837, Ro 08-2750, PPADS, suramin, CGP55845, MRS2279, 3-MATIDA, MPEP, gabazine and ionomycin were from Tocris; CNQX, bicuculline and muscimol from Ascent Scientific; DL-APV, KA, cyclothiazide, GABA and picrotoxin from Sigma; TTX from Alomone Labs; and tetanus toxin from Calbiochem.

Data analysis

Summary data are given as mean±s.e.m. unless otherwise stated. Experimental groups were tested for normality using the Shapiro–Wilk test and subsequently compared using either ANOVA followed by Tukey's HSD for Gaussian data, or Kruskal–Wallis test followed by Dunn–Holland–Wolfe for non-Gaussian data. Speed, displacement and directionality were compared based on their medians to account for their non-normal distribution. Effect size was calculated as follows:

$$\text{effect size (\%)} = 100\% - \frac{\text{median of variable under blocked conditions}}{\text{median of variable under control conditions}} \times 100\%.$$

Development (2017) 144, 4125-4136 doi:10.1242/dev.154096

Percentile-based 95% confidence intervals for medians (Fig. S5D) and effect sizes (Fig. 6) were obtained by bootstrapping using 3000 repetitions. Angular distributions were compared by applying Kuiper's test. Test power was estimated post-hoc using GPower 3.1 if applicable. All statistical procedures were implemented in R (R Development Core Team, 2017).

Acknowledgements
We thank R. Fimmers for advice on statistics and D. Krauss and N. Haias for animal husbandry.

Competing interests
The authors declare no competing or financial interests.

Author contributions
Conceptualization: A.K.W., C.S., K.S., R.J.; Methodology: A.K.W., C.H., D.A.F., J.J.L.v.d.W., K.S., R.J.; Software: A.K.W., D.A.F., K.S., R.J.; Validation: A.K.W., J.J.L.v.d.W., F.A.C., C.S., K.S., R.J.; Formal analysis: A.K.W., C.H., N.B.T., D.A.F., A.T., J.J.L.v.d.W., F.A.C., K.S., R.J.; Investigation: A.K.W., C.H., N.B.T., D.A.F., A.T., J.J.L.v.d.W., F.A.C., R.J.; Resources: J.J.L.v.d.W., F.A.C., C.S., K.S.; Data curation: A.K.W., C.H., C.S., K.S., R.J.; Writing - original draft: A.K.W., C.S., K.S., R.J.; Writing - review & editing: A.K.W., C.H., J.J.L.v.d.W., F.A.C., C.S., K.S., R.J.; Visualization: A.K.W., N.B.T., A.T., J.J.L.v.d.W., F.A.C., K.S., R.J.; Supervision: C.S., K.S., R.J.; Project administration: K.S., R.J.; Funding acquisition: C.S., K.S., R.J.

Funding
This work was supported by grants from the Deutsche Forschungsgemeinschaft (GRK246 to K.S. and A.K.W.; SPP1757: STE 552/5 to C.S., JA 942-1 and JA 942-2 to R.J.) and the European Union Horizon 2020 Framework Programme (ERA-NET NEURON: BrIE to C.S.).

Supplementary information
Supplementary information available online at
http://dev.biologists.org/lookup/doi/10.1242/dev.154096.supplemental

References
Ashwell, K. W. S. and Zhang, L.-L. (1992). Ontogeny of afferents to the fetal rat cerebellum. *Acta Anat. (Basel)* **145**, 17-23.
Barkovich, A. J., Guerrini, R., Kuzniecky, R. I., Jackson, G. D. and Dobyns, W. B. (2012). A developmental and genetic classification for malformations of cortical development: update 2012. *Brain* **135**, 1348-1369.
Batini, C., Compoint, C., Buisseret-Delmas, C., Daniel, H. and Guegan, M. (1992). Cerebellar nuclei and the nucleocortical projections in the rat: retrograde tracing coupled to GABA and glutamate immunohistochemistry. *J. Comp. Neurol.* **315**, 74-84.
Batschelet, E. (1981). *Circular Statistics in Biology*. New York: Academic Press.
Bell, C. C., Han, V. and Sawtell, N. B. (2008). Cerebellum-like structures and their implications for cerebellar function. *Annu. Rev. Neurosci.* **31**, 1-24.
Ben-Arie, N., Bellen, H. J., Armstrong, D. L., McCall, A. E., Gordadze, P. R., Guo, Q., Matzuk, M. M. and Zoghbi, H. Y. (1997). Math1 is essential for genesis of cerebellar granule neurons. *Nature* **390**, 169-172.
Benhamou, S. (2004). How to reliably estimate the tortuosity of an animal's path: straightness, sinuosity, or fractal dimension? *J. Theor. Biol.* **229**, 209-220.
Bolteus, A. J. and Bordey, A. (2004). GABA release and uptake regulate neuronal precursor migration in the postnatal subventricular zone. *J. Neurosci.* **24**, 7623-7631.
Bortone, D. and Polleux, F. (2009). KCC2 expression promotes the termination of cortical interneuron migration in a voltage-sensitive calcium-dependent manner. *Neuron* **62**, 53-71.
Boulland, J.-L., Rafiki, A., Levy, L. M., Storm-Mathisen, J. and Chaudhry, F. A. (2003). Highly differential expression of SN1, a bidirectional glutamine transporter, in astroglia and endothelium in the developing rat brain. *Glia* **41**, 260-275.
Bouzigues, C., Morel, M., Triller, A. and Dahan, M. (2007). Asymmetric redistribution of GABA receptors during GABA gradient sensing by nerve growth cones analyzed by single quantum dot imaging. *Proc. Natl. Acad. Sci. USA* **104**, 11251-11256.
Broeke, J. H. P., Roelandse, M., Luteijn, M. J., Boiko, T., Matus, A., Toonen, R. F. and Verhage, M. (2010). Munc18 and Munc13 regulate early neurite outgrowth. *Biol. Cell* **102**, 479-488.
Cameron, D. B., Kasai, K., Jiang, Y., Hu, T., Saeki, Y. and Komuro, H. (2009). Four distinct phases of basket/stellate cell migration after entering their final destination (the molecular layer) in the developing cerebellum. *Dev. Biol.* **332**, 309-324.
Carter, A. G. and Regehr, W. G. (2002). Quantal events shape cerebellar interneuron firing. *Nat. Neurosci.* **5**, 1309-1318.
Costes, S. V., Daelemans, D., Cho, E. H., Dobbin, Z., Pavlakis, G. and Lockett, S. (2004). Automatic and quantitative measurement of protein-protein colocalization in live cells. *Biophys. J.* **86**, 3993-4003.
Cuzon, V. C., Yeh, P. W., Cheng, Q. and Yeh, H. H. (2006). Ambient GABA promotes cortical entry of tangentially migrating cells derived from the medial ganglionic eminence. *Cereb. Cortex* **16**, 1377-1388.
de Lima, A. D., Gieseler, A. and Voigt, T. (2009). Relationship between GABAergic interneurons migration and early neocortical network activity. *Dev. Neurobiol.* **69**, 105-123.
Dieudonné, S. (1995). Glycinergic synaptic currents in Golgi cells of the rat cerebellum. *Proc. Natl. Acad. Sci. USA* **92**, 1441-1445.
Dieudonné, S. (1998). Submillisecond kinetics and low efficacy of parallel fibre-Golgi cell synaptic currents in the rat cerebellum. *J. Physiol.* **510**, 845-866.
Elisabetta Cesana, L. F., Mapelli, J. and D'Angelo, E. (2006). Ionic mechanisms of autorhythmic firing in rat cerebellar Golgi cells. *J. Physiol.* **574**, 711-729.
Ge, S., Goh, E. L. K., Sailor, K. A., Kitabatake, Y., Ming, G.-L. and Song, H. (2006). GABA regulates synaptic integration of newly generated neurons in the adult brain. *Nature* **439**, 589-593.
Gianola, S., Savio, T., Schwab, M. E. and Rossi, F. (2003). Cell-autonomous mechanisms and myelin-associated factors contribute to the development of purkinje axon intracortical plexus in the rat cerebellum. *J. Neurosci.* **23**, 4613-4624.
Glassmann, A., Topka, S., Wang-Eckardt, L., Anders, S., Weisheit, G., Endl, E., Zimmer, A. and Schilling, K. (2009). Basic molecular fingerprinting of immature cerebellar cortical inhibitory interneurons and their precursors. *Neuroscience* **159**, 69-82.
Goldowitz, D. and Hamre, K. (1998). The cells and molecules that make a cerebellum. *Trends Neurosci.* **21**, 375-382.
Grishkat, H. L. and Eisenman, L. M. (1995). Development of the spinocerebellar projection in the prenatal mouse. *J. Comp. Neurol.* **363**, 93-108.
Hecht, I., Skoge, M. L., Charest, P. G., Ben-Jacob, E., Firtel, R. A., Loomis, W. F., Levine, H. and Rappel, W.-J. (2011). Activated membrane patches guide chemotactic cell motility. *PLoS Comput. Biol.* **7**, e1002044.
Ikin, A. F., Annaert, W. G., Takei, K., Camilli, P. D., Jahn, R., Greengard, P. and Buxbaum, J. D. (1996). Alzheimer amyloid protein precursor is localized in nerve terminal preparations to Rab5-containing vesicular organelles distinct from those implicated in the synaptic vesicle pathway. *J. Biol. Chem.* **271**, 31783-31786.
Jones, M. C., Marron, J. S. and Sheather, S. J. (1996). A brief survey of bandwidth selection for density estimation. *J. Am. Stat. Assoc.* **91**, 401-407.
Jörntell, H., Bengtsson, F., Schonewille, M. and De Zeeuw, C. I. (2010). Cerebellar molecular layer interneurons - computational properties and roles in learning. *Trends Neurosci.* **33**, 524-532.
Jossin, Y. and Cooper, J. A. (2011). Reelin, Rap1 and N-cadherin orient the migration of multipolar neurons in the developing neocortex. *Nat. Neurosci.* **14**, 697-703.
Kalinovsky, A., Boukhtouche, F., Blazeski, R., Bornmann, C., Suzuki, N., Mason, C. A. and Scheiffele, P. (2011). Development of axon-target specificity of ponto-cerebellar afferents. *PLoS Biol.* **9**, e1001013.
Kepecs, A. and Fishell, G. (2014). Interneuron cell types are fit to function. *Nature* **505**, 318-326.
Kim, J., Lee, S., Tsuda, S., Zhang, X., Asrican, B., Gloss, B., Feng, G. and Augustine, G. J. (2014). Optogenetic mapping of cerebellar inhibitory circuitry reveals spatially biased coordination of interneurons via electrical synapses. *Cell Rep.* **7**, 1601-1613.
Kita, Y., Tanaka, K. and Murakami, F. (2015). Specific labeling of climbing fibers shows early synaptic interactions with immature Purkinje cells in the prenatal cerebellum. *Dev. Neurobiol.* **75**, 927-934.
Komuro, H. and Rakic, P. (1993). Modulation of neuronal migration by NMDA receptors. *Science* **260**, 95-97.
Letinic, K., Zoncu, R. and Rakic, P. (2002). Origin of GABAergic neurons in the human neocortex. *Nature* **417**, 645-649.
Leto, K., Bartolini, A., Yanagawa, Y., Obata, K., Magrassi, L., Schilling, K. and Rossi, F. (2009). Laminar fate and phenotype specification of cerebellar GABAergic interneurons. *J. Neurosci.* **29**, 7079-7091.
Leto, K., Bartolini, A., Di Gregorio, A., Imperiale, D., De Luca, A., Parmigiani, E., Filipkowski, R. K., Kaczmarek, L. and Rossi, F. (2011). Modulation of cell-cycle dynamics is required to regulate the number of cerebellar GABAergic interneurons and their rhythm of maturation. *Development* **138**, 3463-3472.
Leto, K., Arancillo, M., Becker, E. B. E., Buffo, A., Chiang, C., Ding, B., Dobyns, W. B., Dusart, I., Haldipur, P., Hatten, M. E. et al. (2016). Consensus paper: cerebellar development. *Cerebellum* **15**, 789-828.
Liu, S. J. and Cull-Candy, S. G. (2002). Activity-dependent change in AMPA receptor properties in cerebellar stellate cells. *J. Neurosci.* **22**, 3881-3889.
Liu, X., Wang, Q., Haydar, T. F. and Bordey, A. (2005). Nonsynaptic GABA signaling in postnatal subventricular zone controls proliferation of GFAP-expressing progenitors. *Nat. Neurosci.* **8**, 1179-1187.
Liu, H.-T., Akita, T., Shimizu, T., Sabirov, R. Z. and Okada, Y. (2009). Bradykinin-induced astrocyte–neuron signalling: glutamate release is mediated by ROS-activated volume-sensitive outwardly rectifying anion channels. *J. Physiol.* **587**, 2197-2209.

LoTurco, J. J., Owens, D. F., Heath, M. J. S., Davis, M. B. E. and Kriegstein, A. R. (1995). GABA and glutamate depolarize cortical progenitor cells and inhibit DNA synthesis. *Neuron* **15**, 1287-1298.
Luhmann, H. J., Fukuda, A. and Kilb, W. (2015). Control of cortical neuronal migration by glutamate and GABA. *Front. Cell. Neurosci.* **9**, 4.
Machold, R. and Fishell, G. (2005). Math1 is expressed in temporally discrete pools of cerebellar rhombic-lip neural progenitors. *Neuron* **48**, 17-24.
Manent, J.-B. and Represa, A. (2007). Neurotransmitters and brain maturation: early paracrine actions of GABA and glutamate modulate neuronal migration. *Neuroscientist* **13**, 268-279.
Manent, J.-B., Demarque, M., Jorquera, I., Pellegrino, C., Ben-Ari, Y., Aniksztejn, L. and Represa, A. (2005). A noncanonical release of GABA and glutamate modulates neuronal migration. *J. Neurosci.* **25**, 4755-4765.
Maricich, S. M. and Herrup, K. (1999). Pax-2 expression defines a subset of GABAergic interneurons and their precursors in the developing murine cerebellum. *J. Neurobiol.* **41**, 281-294.
Marín, O., Valiente, M., Ge, X. and Tsai, L.-H. (2010). Guiding neuronal cell migrations. *Cold Spring Harb. Perspect. Biol.* **2**, a001834.
Markram, H., Toledo-Rodriguez, M., Wang, Y., Gupta, A., Silberberg, G. and Wu, C. (2004). Interneurons of the neocortical inhibitory system. *Nat. Rev. Neurosci.* **5**, 793-807.
Mason, C. A. and Gregory, E. (1984). Postnatal maturation of cerebellar mossy and climbing fibers: transient expression of dual features on single axons. *J. Neurosci.* **4**, 1715-1735.
Matsui, K. and Jahr, C. E. (2004). Differential control of synaptic and ectopic vesicular release of glutamate. *J. Neurosci.* **24**, 8932-8939.
Monyer, H., Seeburg, P. H. and Wisden, W. (1991). Glutamate-operated channels: developmentally early and mature forms arise by alternative splicing. *Neuron* **6**, 799-810.
Naoki, H., Nishiyama, M., Togashi, K., Igarashi, Y., Hong, K. and Ishii, S. (2016). Multi-phasic bi-directional chemotactic responses of the growth cone. *Sci. Rep.* **6**, 36256.
Nunes, M. L. A. and Sotelo, C. (1985). Development of the spinocerebellar system in the postnatal rat. *J. Comp. Neurol.* **237**, 291-306.
Partin, K. M., Patneau, D. K., Winters, C. A., Mayer, M. L. and Buonanno, A. (1993). Selective modulation of desensitization at AMPA versus kainate receptors by cyclothiazide and concanavalin A. *Neuron* **11**, 1069-1082.
Peñagarikano, O., Abrahams, B. S., Herman, E. I., Winden, K. D., Gdalyahu, A., Dong, H., Sonnenblick, L. I., Gruver, R., Almajano, J., Bragin, A. et al. (2011). Absence of CNTNAP2 leads to epilepsy, neuronal migration abnormalities, and core autism-related deficits. *Cell* **147**, 235-246.
Pfeffer, P. L., Payer, B., Reim, G., di Magliano, M. P. and Busslinger, M. (2002). The activation and maintenance of Pax2 expression at the mid-hindbrain boundary is controlled by separate enhancers. *Development* **129**, 307-318.
Puro, D. G. and Woodward, D. J. (1977). Maturation of evoked mossy fiber input to rat cerebellar Purkinje cells (II.). *Exp. Brain Res.* **28**, 427-441.
Raiteri, L. and Raiteri, M. (2015). Multiple functions of neuronal plasma membrane neurotransmitter transporters. *Prog. Neurobiol.* **134**, 1-16.
Rakic, P. (1972). Extrinsic cytological determinants of basket and stellate cell dendritic pattern in the cerebellar molecular layer. *J. Comp. Neurol.* **146**, 335-354.
R Development Core Team (2017). *R: a Language and Environment for Statistical Computing*. Vienna, Austria: R Foundation for Statistical Computing.
Rice, D. S. and Curran, T. (2001). Role of the reelin signaling pathway in central nervous system development. *Annu. Rev. Neurosci.* **24**, 1005-1039.
Rivière, J.-B., van Bon, B. W. M., Hoischen, A., Kholmanskikh, S. S., O'Roak, B. J., Gilissen, C., Gijsen, S., Sullivan, C. T., Christian, S. L., Abdul-Rahman, O. A. et al. (2012). De novo mutations in the actin genes ACTB and ACTG1 cause Baraitser-Winter syndrome. *Nat. Genet.* **44**, 440-4S2.
Ruigrok, T. J. H., Hensbroek, R. A. and Simpson, J. I. (2011). Spontaneous activity signatures of morphologically identified interneurons in the vestibulocerebellum. *J. Neurosci.* **31**, 712-724.
Rymar, V. V. and Sadikot, A. F. (2007). Laminar fate of cortical GABAergic interneurons is dependent on both birthdate and phenotype. *J. Comp. Neurol.* **501**, 369-380.
Sassoe-Pognetto, M. and Patrizi, (2013). Development of Glutamatergic and GABAergic Synapses. In *Handbook of Cerebellum and Cerebellar Disorders*, pp. 237-255. Dordrecht: Springer.
Schilling, K. (2013). Specification and development of GABAergic interneurons. In *Handbook of the Cerebellum and Cerebellar Disorders* (ed. M. Manto, D. L. Gruol, J. D. Schmahmann, N. Koibuchi and F. Rossi), pp. 207-235. New York: Springer.
Schilling, K., Oberdick, J., Rossi, F. and Baader, S. L. (2008). Besides Purkinje cells and granule neurons: an appraisal of the cell biology of the interneurons of the cerebellar cortex. *Histochem. Cell Biol.* **130**, 601-615.
Sheather, S. J. and Jones, M. C. (1991). A reliable data-based bandwidth selection method for kernel density estimation. *J. R. Stat. Soc. Ser. B Stat. Methodol.* **53**, 683-690.
Shimono, T., Nosaka, S. and Sasaki, K. (1976). Electrophysiological study on the postnatal development of neuronal mechanisms in the rat cerebellar cortex. *Brain Res.* **108**, 279-294.
Simat, M., Ambrosetti, L., Lardi-Studler, B. and Fritschy, J.-M. (2007). GABAergic synaptogenesis marks the onset of differentiation of basket and stellate cells in mouse cerebellum. *Eur. J. Neurosci.* **26**, 2239-2256.
Smith, T. C., Wang, L.-Y. and Howe, J. R. (2000). heterogeneous conductance levels of native AMPA receptors. *J. Neurosci.* **20**, 2073-2085.
Sokoloff, G., Plumeau, A. M., Mukherjee, D. and Blumberg, M. S. (2015). Twitch-related and rhythmic activation of the developing cerebellar cortex. *J. Neurophysiol.* **114**, 1746-1756.
Southan, A. P. and Robertson, B. (1998). Patch-clamp recordings from cerebellar basket cell bodies and their presynaptic terminals reveal an asymmetric distribution of voltage-gated potassium channels. *J. Neurosci.* **18**, 948-955.
Spitzer, N. C. (2006). Electrical activity in early neuronal development. *Nature* **444**, 707-712.
Sudarov, A., Turnbull, R. K., Kim, E. J., Lebel-Potter, M., Guillemot, F. and Joyner, A. L. (2011). Ascl1 genetics reveals insights into cerebellum local circuit assembly. *J. Neurosci.* **31**, 11055-11069.
Sultan, F. and Bower, J. M. (1998). Quantitative Golgi study of the rat cerebellar molecular layer interneurons using principal component analysis. *J. Comp. Neurol.* **393**, 353-373.
Tan, S.-S., Kalloniatis, M., Sturm, K., Tam, P. P. L., Reese, B. E. and Faulkner-Jones, B. (1998). Separate progenitors for radial and tangential cell dispersion during development of the cerebral neocortex. *Neuron* **21**, 295-304.
Valiente, M. and Marín, O. (2010). Neuronal migration mechanisms in development and disease. *Curr. Opin. Neurobiol.* **20**, 68-78.
van den Pol, A. N. and Gorcs, T. (1986). Synaptic relationships between neurons containing vasopressin, gastrin-releasing peptide, vasoactive intestinal polypeptide, and glutamate decarboxylase immunoreactivity in the suprachiasmatic nucleus: Dual ultrastructural immunocytochemistry with gold-substituted silver peroxidase. *J. Comp. Neurol.* **252**, 507-521.
Verderio, C., Coco, S., Bacci, A., Rossetto, O., Camilli, P. D., Montecucco, C. and Matteoli, M. (1999). Tetanus toxin blocks the exocytosis of synaptic vesicles clustered at synapses but not of synaptic vesicles in isolated axons. *J. Neurosci.* **19**, 6723-6732.
Wassef, M., Chedotal, A., Cholley, B., Thomasset, M., Heizmann, C. W. and Sotelo, C. (1992). Development of the olivocerebellar projection in the rat: I. Transient biochemical compartmentation of the inferior olive. *J. Comp. Neurol.* **323**, 519-536.
Watanabe, M. and Kano, M. (2011). Climbing fiber synapse elimination in cerebellar Purkinje cells. *Eur. J. Neurosci.* **34**, 1697-1710.
Watt, A. J., Cuntz, H., Mori, M., Nusser, Z., Sjöström, P. J. and Häusser, M. (2009). Traveling waves in developing cerebellar cortex mediated by asymmetrical Purkinje cell connectivity. *Nat. Neurosci.* **12**, 463-473.
Weisheit, G., Gliem, M., Endl, E., Pfeffer, P. L., Busslinger, M. and Schilling, K. (2006). Postnatal development of the murine cerebellar cortex: formation and early dispersal of basket, stellate and Golgi neurons. *Eur. J. Neurosci.* **24**, 466-478.
Xiong, Y., Huang, C.-H., Iglesias, P. A. and Devreotes, P. N. (2010). Cells navigate with a local-excitation, global-inhibition-biased excitable network. *Proc. Natl. Acad. Sci. USA* **107**, 17079-17086.
Zhang, L. and Goldman, J. E. (1996). Generation of cerebellar interneurons from dividing progenitors in white matter. *Neuron* **16**, 47-54.

Supplementary Figures

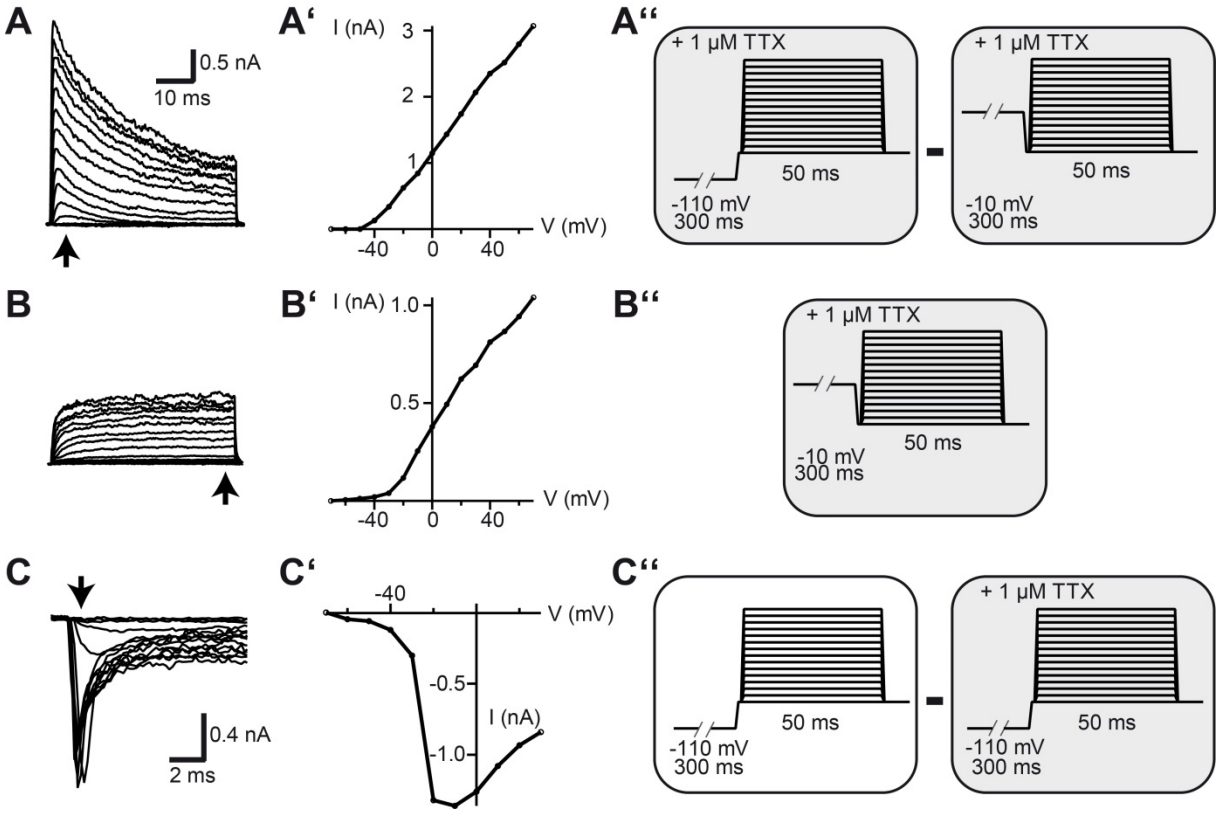

Fig. S1: Pax-2 cells express voltage-gated K^+ and Na^+ channels. Whole-cell membrane currents (A–C) were activated by application of the illustrated voltage step protocols in the presence or absence of 1 µM TTX (A’’–C’’, depolarization between −70 and +70 mV; 10 mV increments, conditioning pre-pulses to −110 mV or −10 mV, respectively, trace family subtraction as indicated in the scheme; n = 3 cells analysed). Arrows in A–C indicate the time points used for the generation of corresponding I/V relations (A’–C’). For whole-cell current pattern see Fig. 3A.

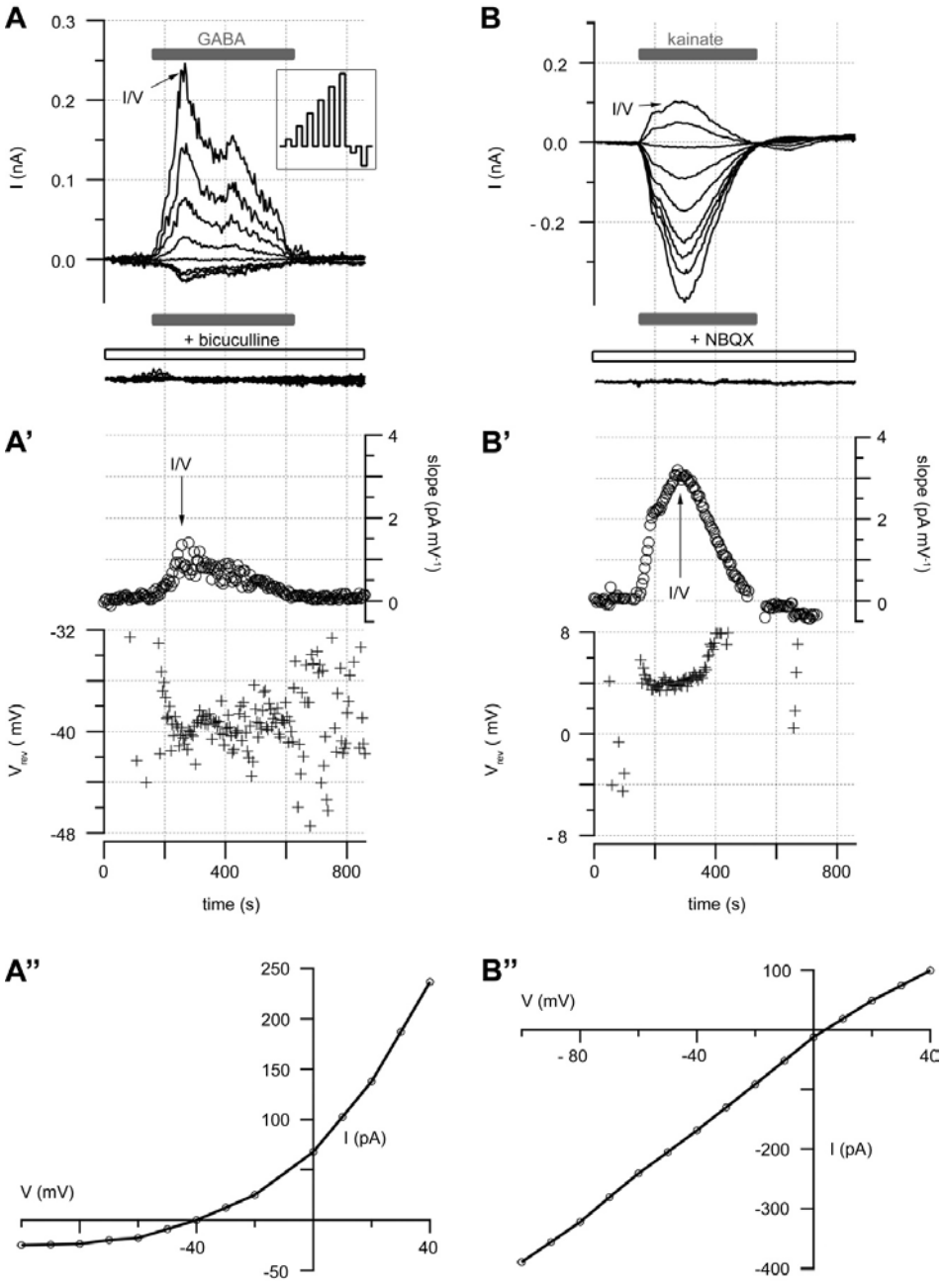

Fig. S2: Pax2-cells express $GABA_A$ - and AMPA/KA- receptors. (A) Time course of GABA- (100 µM) induced currents observed at holding potentials ranging from −100 to +40 mV (100 ms duration; inset: voltage protocol; n = 14 cells analysed plus n = 13 with application of the $GABA_A$-receptor agonist muscimol). Co-application of 100 µM bicuculline blocked GABA-induced currents (bottom; n = 4 cells each analysed with GABA and muscimol). (B) 300 µM KA-induced currents (same protocol as in A; n = 14 cells analysed) were blocked by 10 µM NBQX (bottom; n = 8 cells analysed). (A',B') Time course of slope conductances (top, circles) and reversal potentials (bottom, crosses) for GABA- (A') and KA- (B') induced currents. (A'',B'') I/V-curves for GABA- (reversal potential −40 mV) and KA- (reversal potential 4 mV) responses, taken at maximal receptor activation (arrow in A' and B', respectively). Note: The non-linear $GABA_A$ I/V plot might be a consequence of significant receptor desensitization that can occur by slow solution exchange typical for bath application.

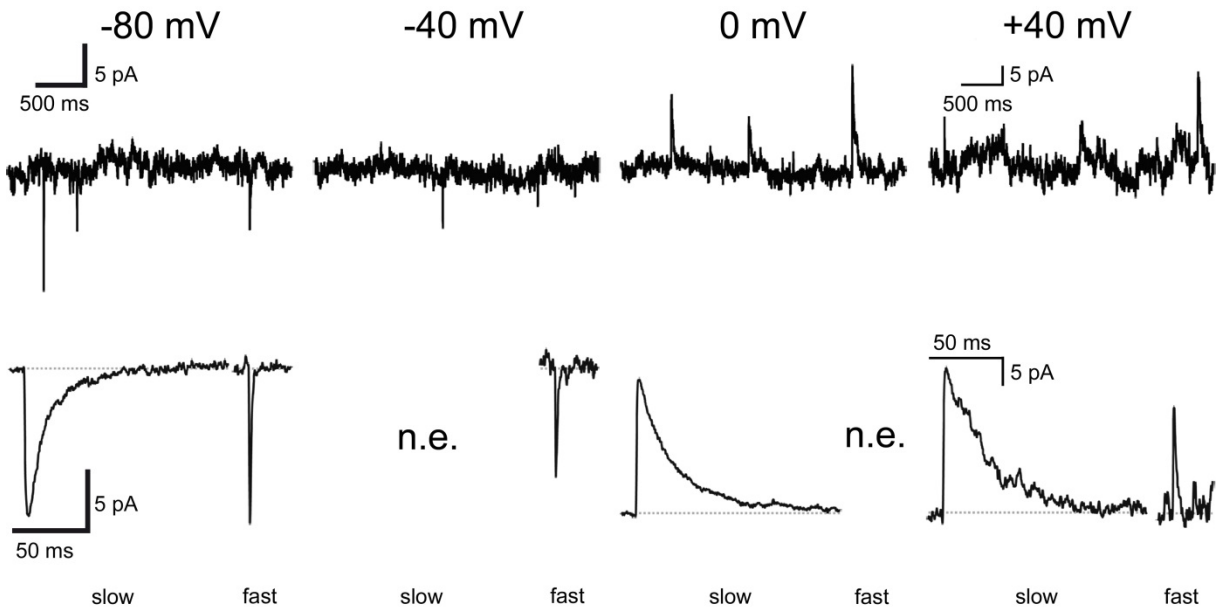

Fig. S3: Ionic nature of slow and fast sPSCs. Top: Current traces recorded at the holding potentials indicated. Bottom: Corresponding averaged slow (left) and fast (right) sPSCs. Slow sPSCs are absent at −40 mV (reversal potential for Cl^-; n.e. non-existent). Fast sPSCs are absent at 0 mV, indicating non-selective cation channels. n = 32 Pax2-cells were analysed for synaptic innervation with this protocol.

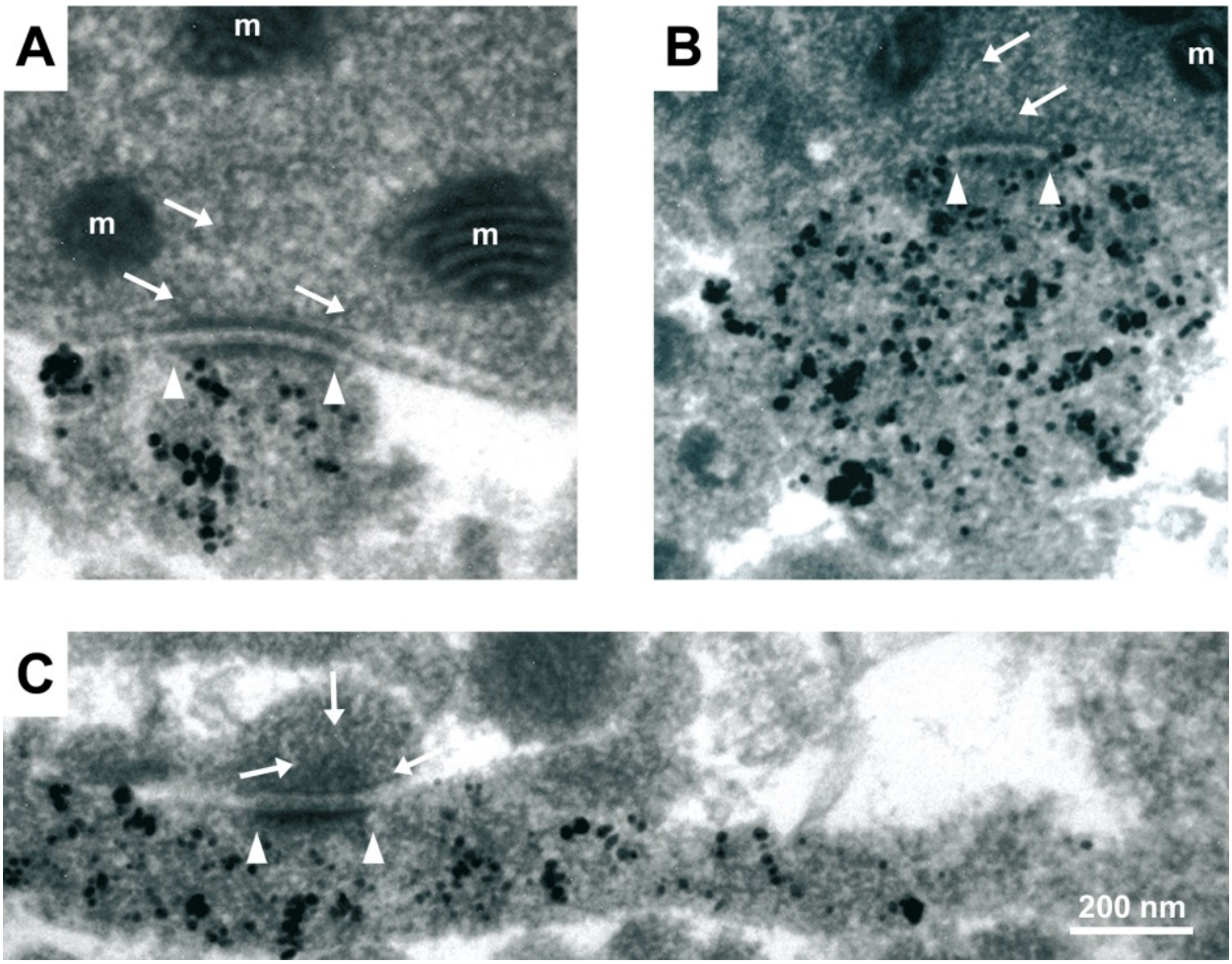

Fig. S4: Pax2-cells in the lower ML form symmetric and asymmetric synapses. Intensification of the GFP-immunosignal using a gold-substituted silver peroxidase technique results in electron-dense granula that facilitate the identification of Pax2-EGFP-positive structures, but it somewhat obscures synaptic vesicles. Both symmetric (A,B) and asymmetric (C) synapses may be discerned on EGFP-immunopositive Pax2-cells. Arrowheads demarcate postsynaptic densities, arrows hint at presynaptic vesicles.

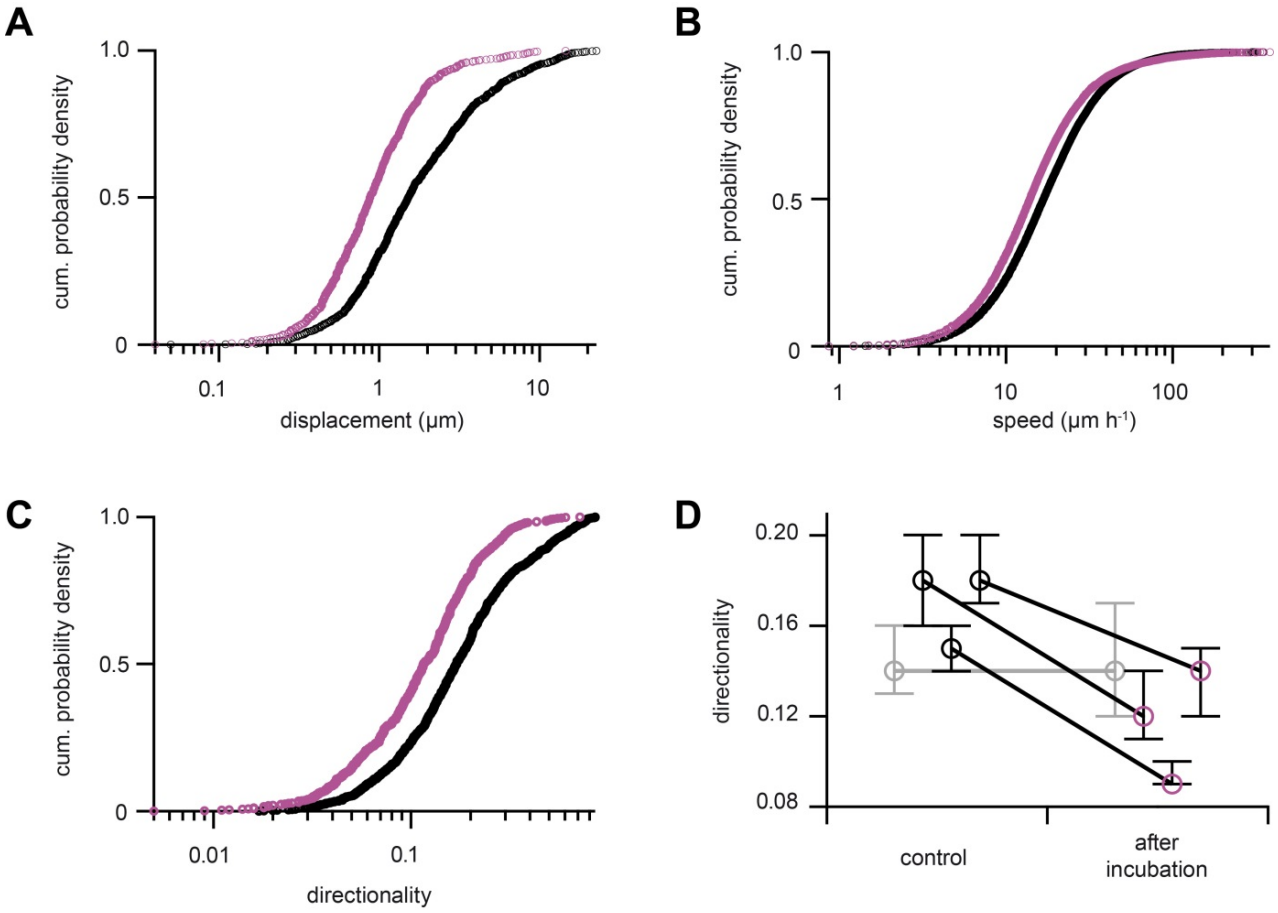

Fig. S5: Details of the TeNT-induced effects on Pax2-cell migration. Displacement (A), speed (B) and directionality (C) of Pax2-cells, recorded in three slices before (917 cells in total, black circles) and following tetanus toxin (TeNT) treatment (100 µg/ml, 2 h; 651 cells, magenta circles; x-axis in logarithmic scale). TeNT reduced median displacement (A) by 42.4% (95% confidence interval (CI) 37.7 to 45.0%; bootstrapping), while the effect on speed (B) was less (17.0%; 95% CI 16.1 to 18%). This predominant effect of TeNT on displacement is a consequence of reduced directionality (C 29.4%; 95% CI 23.5 to 35.3%). Inter-experimental reproducibility is documented in panel D, where TeNT-induced reduction of directionality in individual slices (i.e., independent experiments, n = 3) is shown (black) together with a sham-incubated control slice (grey). In each slice, between 198 and 319 control and TeNT-treated cells were analyzed.

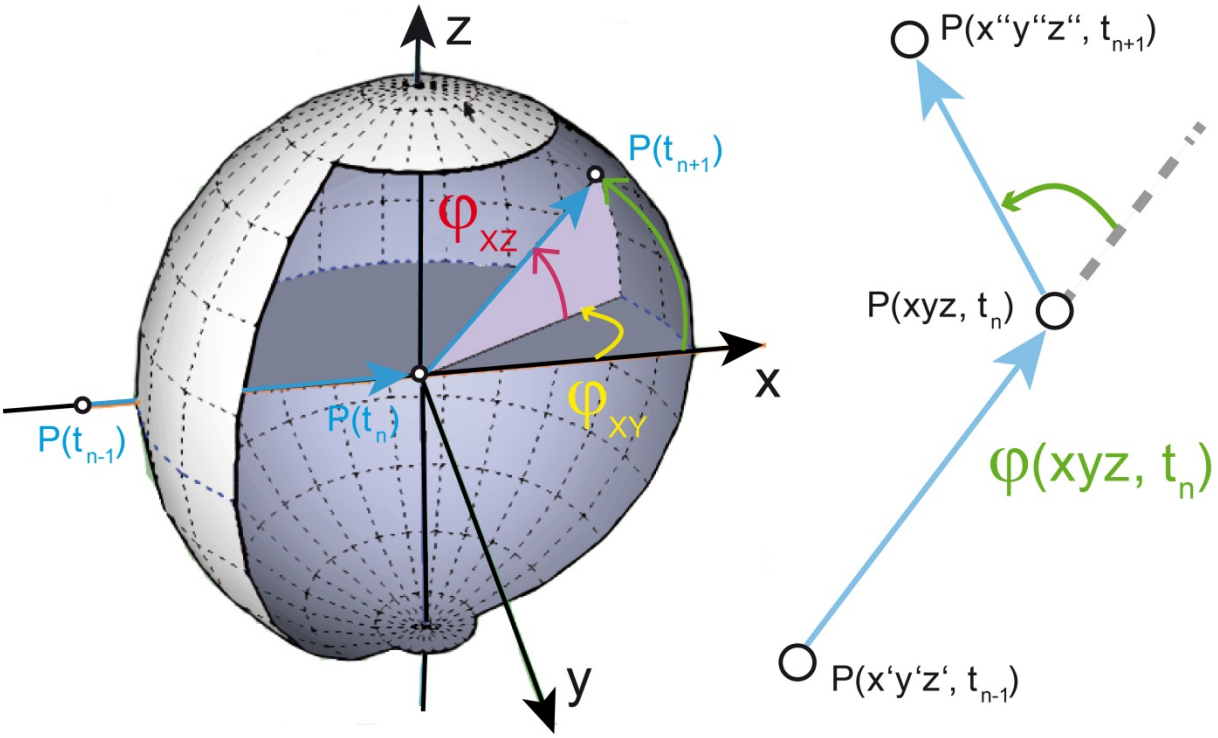

Fig. S6: Scheme of angular measurements. Pax2-cell migration was observed as sequence of mass center positions at discrete time points P(t). Directional persistence was assessed by measuring the angle formed by two subsequent migration steps. Thus, the angle associated with the time point t_n is defined by the three subsequent positions $P(t_{n-1})$, $P(t_n)$ and $P(t_{n+1})$) and the two vectors they form ($(\overrightarrow{P(t_{n-1})\,P(t_n)}$ *and* $\overrightarrow{P(t_n)\,P(t_{n+1})}$, blue). For the results shown in Fig. 7A,A’,B,B’,C,C’ projections in the sagittal and coronal planes yielded angular components φ_{xy} (yellow) and φ_{xz} (red). To obtain a univariate measure of directional persistence suitable for formal statistical testing, we calculated the dot product (i.e. scalar, or inner product) of the vectors defining φ_{xy} and φ_{xz} which yields φ_{xyz} (green, see Fig. 7A’’,B’’,C’’).

Movies

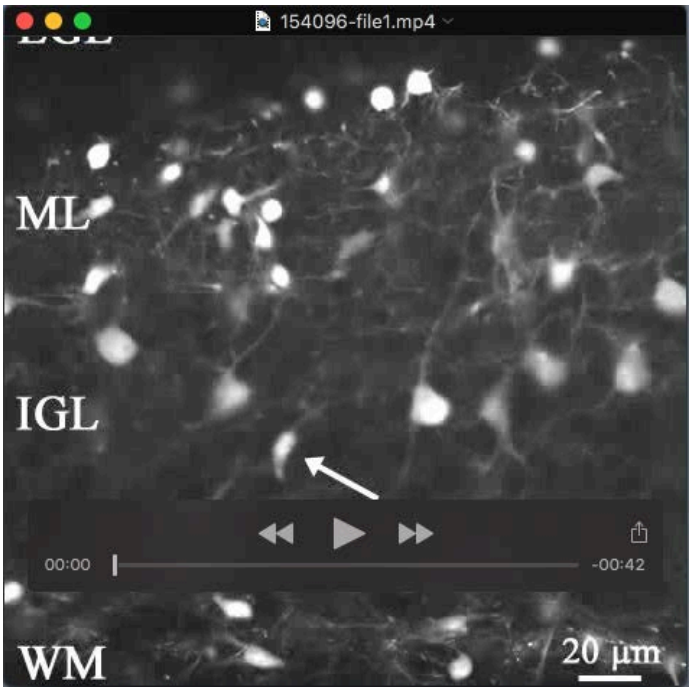

Movie 1. A Pax2-cell migrating across the developing cerebellar cortex. Confocal time lapse recording (cLSM, Pascal 5, Carl Zeiss; frames were taken every 10 seconds for 3 hours) from a sagittal slice obtained from a p7 mouse. Pax2-cells are identified by their expression of EGFP. Large, roundish Pax2-cells in the IGL are resident Golgi cells. Several smaller, mainly bipolar Pax2-cells can be seen to migrate in the prospective WM, the IGL and towards the ML. One of these precursors of ML interneurons can be followed as it migrates from about the middle of the IGL to the outer ML within 3 h. Its initial and final positions are marked by arrows in the first and last frame, respectively. Note that this Pax2-cell repeatedly extends and retracts branches of the leading process and has highly dynamic growth cones. Some jitter in the movie and variable intensities of other cells are due to the fact that we repeatedly re-focused on this one cell during recording.

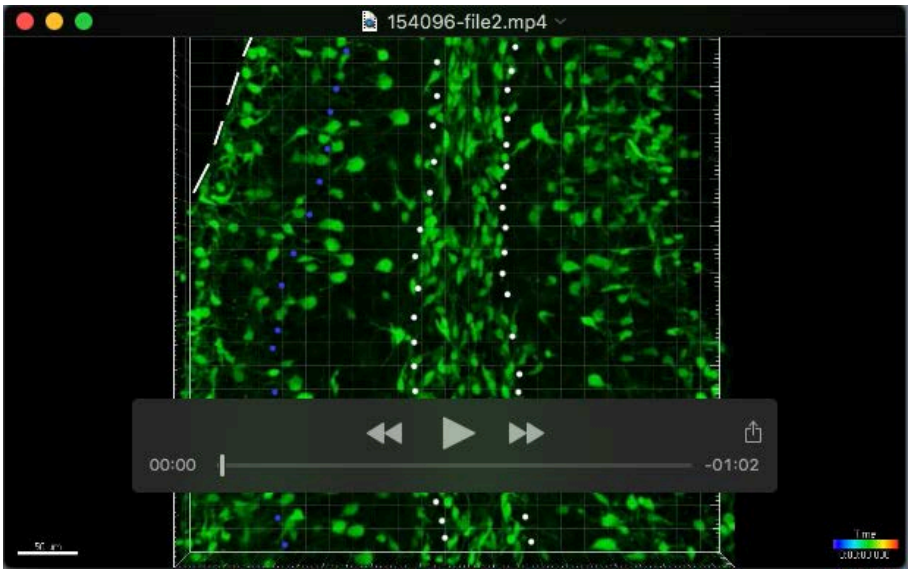

Movie 2. Migration of Pax2-cells. This movie starts with an overview showing cell motility of Pax2-EGFP positive (green) cells in acute 300 µm thick sagittal slices from lobules IV and V of an 8 day old cerebellum. Rostral is to the right, and dorsal (apical) is towards the top of the frame shown.

In the initial still image, the approximate borders of the white matter (WM) are indicated by white dots. In lobule V, the position of the Purkinje cell layer (PCL) is marked with blue dots, and the inner border of the external granule cell layer (EGL) is indicated by white dashes.

Following this still image, the scene is rotated to give an impression of the three-dimensional arrangement of Pax2-EGFP positive cells. Subsequently, motility of Pax2-cells over a 30 min period is shown. This short sequence is looped over three times. Subsequently, we zoom-in on a region in the more basal part of this lobule (see yellow boxed area in the overview in the top right corner of the movie).

The next sequence again starts with a still image in which the PCL (blue dots) and the inner border of the EGL (white dashed line) are indicated. Three cells marked with red, perpendicular arrowheads will be seen migrating in the subsequent part of the movie. Some immobile cells are labelled with yellow, horizontal arrowheads. The subsequent rotation of the scene shows that the two migratory cells in the inner granule cell layer (here, to the right of the PCL) that appear very close to each other in the standard projection are indeed found at different depth in this slice. Finally, a still image is shown to document how iso-surfaces (labelled whitish-grey), used to calculate the centres of mass of individual Pax2-cells, were fitted to cell volumes. Centres of mass were used to pinpoint cell positions and mobility.

The next sequence shows cell mobility over the complete period of 30 minutes in this region, along with the tracks describing the temporal displacement of the cells. The centres of mass are depicted for every time point as white squares. This scene is replayed three times. Finally, centres of mass and the tracks only are displayed for three loops. Note that the three highly mobile cells in this frame follow more-or-less straight tracks towards the EGL. In the final still image, tracks of the mobile cells marked by red arrowheads are again labelled by red, perpendicular arrowheads. Note that centres of mass of immobile

cells (yellow, horizontal arrowheads) did not move appreciably. Colour coding of the tracks reflects time (scale in the bottom right corner of the movie).

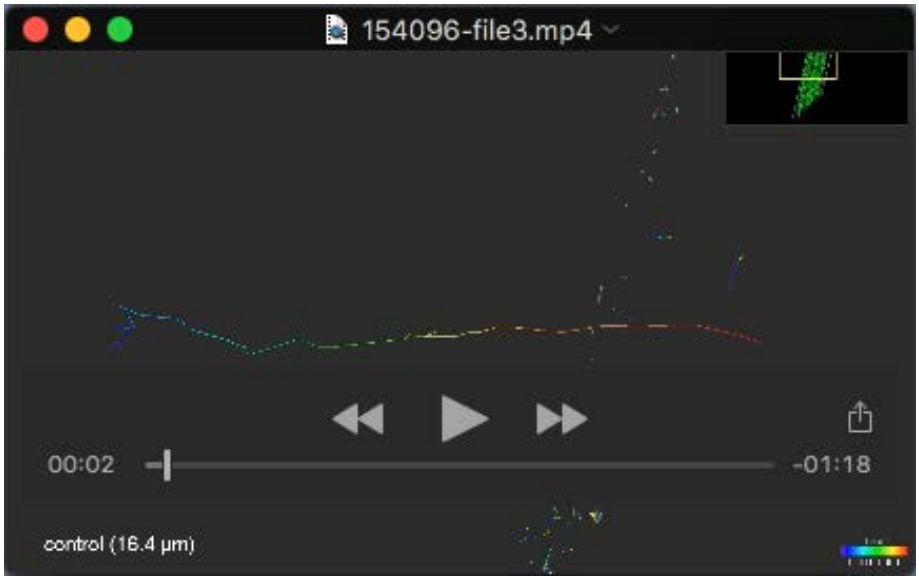

Movie 3. Exemplary tracks of control cells and tetanus toxin-treated cells. In this movie, six pairs of tracks are shown, each consisting of length-matched tracks recorded under control conditions and following incubation with tetanus toxin. Note that under control conditions, tracks are highly directed and typically elongated, though they may also comprise short phases or random, to-and-fro movement. Following treatment with tetanus toxin (TeNT), cells show very little, if any, directional persistence, and individual steps of each track appear more or less randomly oriented. Consequently, the net displacement from the first to the last time point is small as compared to controls.

As the movie does not allow visualizing the true three-dimensional structure of the tracks, we rotated tracks such that their projection to the screen maximises their visible length (see yellow box in the overview scheme at the top right corner for orientation). Treatment condition and three-dimensional track lengths (in µm) are indicated in the stills preceding movie sequences. In some sequences, centres of mass of essentially immobile cells can be seen and may serve as a reference.

The net displacements of these length-matched tracks were as follows (all in µm; controls vs TeNT-treated): 12.8 vs 1.9; 5.1 vs 1.4; 4.4 vs 1.1; 14.5 vs 0.9; 13.2 vs 1.2; 14.9 vs 6.8.